

Going beyond the Borders: Field-of-View Extension in MR/PET Hybrid Imaging

Inauguraldissertation

zur Erlangung der Würde eines Doktors der Philosophie
vorgelegt der
Philosophisch-Naturwissenschaftlichen Fakultät
der Universität Basel

von

Jan Ole Blumhagen
aus Lübeck, Deutschland

Erlangen, 2012

Genehmigt von der Philosophisch-Naturwissenschaftlichen Fakultät
auf Antrag von

Prof. Dr. Klaus Scheffler
Dissertationsleiter

Prof. Dr. Harald Quick
Korreferent

Basel, den 18. September 2012

Prof. Dr. Jörg Schibler
Dekan

Abstract

The recent combination of Magnetic Resonance Imaging (MRI) and Positron Emission Tomography (PET) is of emerging interest in clinical routine. On the one hand, MRI is a widely-used diagnostic tool in medical practice. The excellent soft-tissue contrast offers reliable anatomical information. On the other hand, PET is a key imaging technique in nuclear medicine. It shows the functional metabolism thus providing information on the biochemical and physiological processes of the patient. The recently developed MR/PET hybrid system combines these advantages in one whole-body system.

The integration of the PET detector in an MR system is a new challenge. In particular, new concepts for the attenuation correction of the PET data are required. This attenuation correction can be performed based on the MR data. However, the MR field-of-view (FoV) is limited by intrinsic physical restrictions such as B_0 inhomogeneities and gradient nonlinearities. It has been reported that the PET quantification is biased due to the limitation of the MR-based FoV. Thus, new acquisition techniques are required for imaging beyond the FoV limitation. This was addressed in this thesis.

A novel method was developed to compensate the distortions arising from the gradient nonlinearity and the B_0 inhomogeneity by using an optimal gradient amplitude. This imaging technique was implemented in a spin-echo-based sequence featuring multi-slice acquisition, bipolar readout and continuous table movement. Thereby, an extension of the FoV was achieved. The optimal sequence parameters were determined inline and applied automatically. No further user interaction or hardware modifications were required. The additional acquisition time is easily tolerable for clinical routine.

In a patient study the improvement achieved by the proposed method was verified. The reported bias in the PET reconstruction was reduced significantly. Therefore, the proposed technique improves the MR-based attenuation correction of the PET emission data. Furthermore, the achieved FoV extension might be of interest for diverse MR applications such as image-guided therapy or measuring of large patients. In summary a method has been developed that improves the PET quantification in MR/PET hybrid imaging.

Publications and Patents arising from this Thesis

Journal Papers and Conference Proceedings

- **Blumhagen JO**, Ladebeck R, Fenchel M, Scheffler K. MR-based field-of-view Extension in MR/PET: B_0 Homogenization Using Gradient Enhancement. *Magnetic Resonance in Medicine 2012*, in print.
- **Blumhagen JO**, Ladebeck R, Fenchel M, Kampmeier J, Scheffler K. *MR-based Field-of-View Extension: Compensation of Field Imperfections*. In Proc. 19th Annual Meeting ISMRM, 2011.
- **Blumhagen JO**, Ladebeck R, Fenchel M, Kampmeier J, Scheffler K. *MR-based Field-of-View Extension: Gradient and B_0 Correction Post-Processing*. In Proc. 19th Annual Meeting ISMRM, 2011.
- **Blumhagen JO**, Ladebeck R, Fenchel M, Scheffler K. *MR-based Axial Field-of-View Extension: Bipolar Dual-Echo Spin Echo Imaging Using Automatically Optimized Readout Gradients*. In Proc. 28th Annual Meeting ESMRMB, 2011.
- **Blumhagen JO**, Ladebeck R, Fenchel M, Scheffler K. *Multislice 2D Spin Echo Imaging Using Adapted Readout Gradients for Compensation of B_0 Inhomogeneities and Gradient Nonlinearities*. In Proc. 28th Annual Meeting ESMRMB, 2011.
- **Blumhagen JO**, Ladebeck R, Fenchel M, Scheffler K. *MR-basierte Field-of-View-Vergrößerung in der Ganzkörper-MR/PET*. 14. Jahrestagung der Deutschen Sektion der ISMRM, 2011.
- **Blumhagen JO**, Ladebeck R, Fenchel M, Scheffler K, Quick H. *MR-based FoV Extension in Whole-Body MR/PET Using Continuous Table Move*. In Proc. 20th Annual Meeting ISMRM, 2012.
- **Blumhagen JO**, Ladebeck R, Fenchel M, Quick H, Scheffler K. *MR-based FoV Extension of Human Attenuation Correction in Whole-Body MR/PET Hybrid Imaging*. In Proc. 20th Annual Meeting ISMRM, 2012.

Patents

- **Blumhagen JO**, Ladebeck R, Fenchel M. Field-of-View-Erweiterung zur humanen Schwächungskorrektur in der Ganzkörper-MR-PET durch selektive Schichtauswahl. *Declared 02/2010 (DE), 01/2011 (US, CN). Published 08/2011. Granted 03/2012.*
- **Blumhagen JO**, Ladebeck R, Fenchel M. Field-of-View-Erweiterung zur humanen Schwächungskorrektur in der Ganzkörper-MR-PET durch destruktive Überlagerung der Nichtlinearitäten des Gradientenfeldes mit den Inhomogenitäten des B_0 -Feldes. *Declared 09/2010 (DE), 09/2011 (US, CN). Published 03/2012.*
- **Blumhagen JO**, Ladebeck R, Fenchel M. Biopolare Dual-Echo Spin-Echo-Sequenz mit automatisch optimiertem Readout-Gradient: MR-basierte Field-of-View-Erweiterung zur humanen Schwächungskorrektur in der Ganzkörper-MR-PET. *Declared 03/2011 (DE), 03/2012 (US, CN). Published 09/2012.*
- **Blumhagen JO**, Ladebeck R, Fenchel M. Positionsabhängige MR-Verzeichnungsreduzierung: MultiSlice SpinEcho Imaging mit automatisch optimiertem MultiSlice Readout Gradientenarray in MR-PET. *Declared 09/2011 (DE), 09/2012 (US, CN).*
- **Blumhagen JO**, Quick H, Ladebeck R, Fenchel M. Kombination von optimierter MR Verzeichnungsreduzierung und Continuously Moving-Table Acquisition: MR-basierte Field of View Erweiterung zur humanen Schwächungskorrektur in der Ganzkörper MR-PET. *Declared 09/2011 (DE), 09/2012 (US, CN).*
- **Blumhagen JO**, Kannengießer S. MR-basierte axiale Field-of-View-Erweiterung durch Verzeichnungsreduzierung mittels Tischvorschub. *Declared 07/2012 (DE).*
- **Blumhagen JO**, Ladebeck R, Fenchel M. Erweiterung der MR-basierten humanen Schwächungskorrektur in der Ganzkörper-MR/PET. *Declared 02/2012 (DE).*
- Brinker G, **Blumhagen JO**. Individuelle Skalierung der Berührschutzfunktion. *Declared 03/2012 (DE).*
- **Blumhagen JO**, Ladebeck R, Fenchel M. Workflow-Optimierung zur schnellen FoV-Erweiterung für die humane Schwächungskorrektur in der simultanen Ganzkörper-MR/PET-Bildgebung. *Declared 03/2012 (DE).*
- **Blumhagen JO**, Ladebeck R, Fenchel M. Optimierte Messzeitnutzung bei gated MRI. *Declared 08/2012 (DE).*

Contents

1	Introduction	9
1.1	MR/PET Hybrid Imaging	10
1.1.1	Magnetic Resonance Imaging	10
1.1.2	Positron Emission Tomography	12
1.1.3	Characteristics of MRI and PET	13
1.2	Challenges in MR/PET	13
1.3	MR-based Attenuation Correction	14
1.4	MR-based FoV Extension	15
1.5	Aim and Outline of this Thesis	17
2	Analysis of Hardware-Dependent Geometrical Distortion	23
2.1	Introduction	24
2.2	Theory	25
2.3	Materials and Methods	26
2.3.1	Measurements of Magnetic Fields	26
2.3.2	Simulation of Distortion	26
2.3.3	Phantom Measurements	28
2.4	Results	29
2.4.1	Frequency Mapping	29
2.4.2	In-plane Distortion	30
2.4.3	Through-plane Distortion	31
2.5	Discussion	34
2.6	Conclusion	36
3	A New Method: MR-based Field-of-View Extension in MR/PET	41
3.1	Introduction	42
3.2	Theory	43
3.3	Materials and Methods	44
3.3.1	Simulations	44
3.3.2	Sequence Design	45
3.3.3	Phantom Studies	45
3.3.4	<i>In Vivo</i> Studies	46

3.4	Results	46
3.4.1	Distortion in an extended FoV	46
3.4.2	Field Measurements and Simulations	48
3.4.3	Phantom Experiments	52
3.4.4	Volunteer Experiments	53
3.5	Discussion	55
3.6	Conclusion	57
4	Implementation	61
4.1	Introduction	62
4.2	Materials and Methods	62
4.2.1	Sequence Design 1: Automatic Selection of Optimal Read- out Gradient in Multi-Slice Spin-Echo	62
4.2.2	Sequence Design 2: Bipolar Dual Echo Spin-Echo	64
4.2.3	Sequence Design 3: Continuous Table Movement	64
4.3	Results	66
4.3.1	Multi-Slice Spin-Echo-Based Implementation	66
4.3.2	Bipolar Dual Echo Implementation	67
4.3.3	Continuous Table Movement	67
4.4	Discussion	68
4.5	Conclusion	68
5	Clinical Application and Patient Study: Impact on Quantita- tive PET Reconstruction	71
5.1	Introduction	72
5.2	Materials and Methods	73
5.2.1	MR-based FoV Extension	73
5.2.2	AC Map Completion	75
5.2.3	Impact on the PET Reconstruction	76
5.2.4	Patient Population	78
5.3	Results	79
5.4	Discussion	83
5.5	Conclusion	85
6	Summary and Conclusion	89

Chapter 1

Introduction

In medical diagnosis, magnetic resonance imaging (MRI) has become one of the most important imaging modalities over the last few decades. Since the pioneering work of Mansfield and Lauterbur in 1973 [1, 2], honored by the Nobel Prize in 2003, and the introduction into clinical use in the 1980s, MRI is both essential in clinical routine and subject of an increasing number of fascinating research and further technical developments. MRI is a non-invasive imaging modality. The most commonly used application in clinical routine is the cross-sectional image acquisition of anatomical data. In comparison to different imaging modalities such as Computer Tomography (CT) or Positron Emission Tomography (PET), MRI offers an excellent soft-tissue contrast without the use of ionizing radiation. While MRI has various advantages in distinguishing anatomical structures, PET is required to visualize the functional processes of the body. Particularly in oncology, neuroimaging and cardiology, PET is an important technique. Considering the complementary information provided by MRI and PET a combination into one hybrid system is obvious.

1.1 MR/PET Hybrid Imaging

In multimodal imaging, a recent accomplishment is the successful integration of MRI and PET into one clinical whole-body system for true simultaneous acquisition [3–14]. In contrast to the established PET/CT hybrid imaging modality, the MR/PET hybrid system offers an excellent soft-tissue contrast. Functional and anatomical information can be acquired simultaneously and the radiation-dose of the CT can be spared. Thus, MR/PET is of emerging interest for many clinical applications such as abdominal imaging [15], tumor neuroimaging [16, 17], diffusion tensor imaging [18], prostate cancer [19], cardiac metabolism [20], cardiac function [21] and whole-body oncology [22]. Figure 1.1 shows images from a whole-body MR/PET acquisition.

1.1.1 Magnetic Resonance Imaging

An MR experiment typically employs three types of electromagnetic spin interactions: a strong static magnetic B_0 -field aligns the spin magnetization, MR signal excitation is performed by a radiofrequency B_1 -field and a time-varying gradient field allows for the spatial encoding of the MR signal. In the presence of a homogeneous static magnetic field the energy level of the nuclei splits into sub-levels according to the Zeeman effect. The energy spectrum is quantized with equally spaced energy levels dependent on the strength of the magnetic field

$$E_m = \gamma \hbar m B_0, \quad (1.1)$$

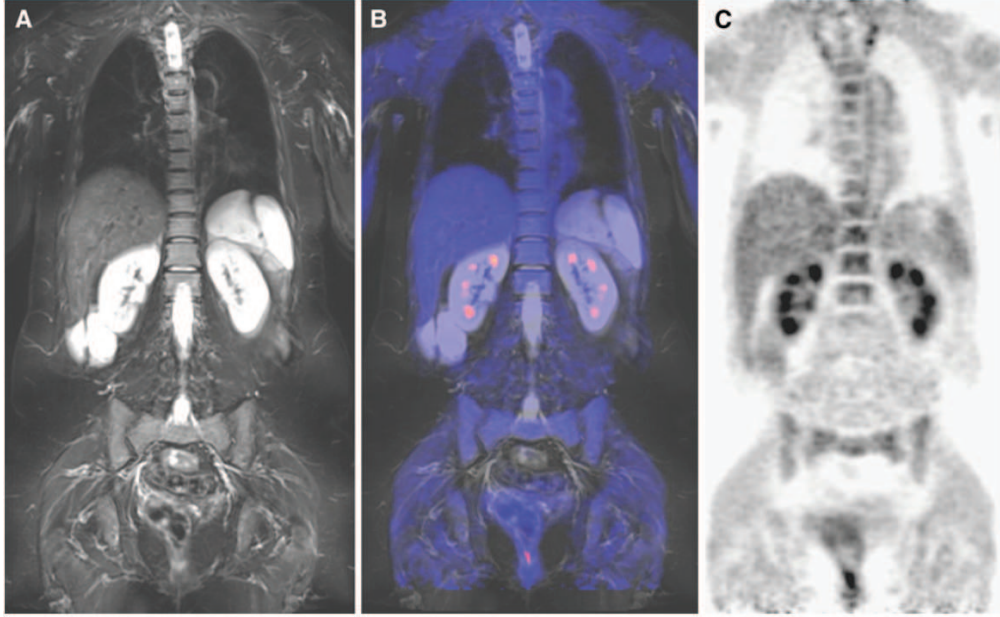


Figure 1.1: Whole-body MR/PET acquisition in a patient with suspicion for tumor recurrence of cervix cancer. Coronal T2 weighted inversion recovery sequence (A). Corresponding superimposition (B). FDG-PET (C). Adapted from [15].

where γ is the gyromagnetic ratio, \hbar the Planck constant, m the quantum number and B_0 the strength of the main magnetic field.

The transition between neighboring energy levels can be induced by the radiofrequency B_1 -field. The energy of the B_1 -field $E_{RF} = \hbar\omega_{RF}$ has to be equal to the difference between the adjacent energy levels to allow such a transition. Thus, the resonance condition is:

$$\omega_{RF} = \omega_0 = \gamma B_0. \quad (1.2)$$

For the image formation it is essential to extract the contribution factor of each voxel from the total signal. Such a spatial encoding of the signal is achieved by three linear space-dependent gradient fields

$$\vec{B}_G = \vec{G} \cdot \vec{r} \quad (1.3)$$

which are superimposed to the static magnetic field. Therefore, the resonance frequency becomes space-dependent and can be described in the rotating frame of reference ($\omega_0=0$) as

$$\omega(\vec{r}) = \gamma \cdot \vec{G} \cdot \vec{r}. \quad (1.4)$$

Thus, the complex MR signal is spatial encoded by the gradient field and can be described as

$$S(t) = \int d^3r \rho(\vec{r}) e^{i(\gamma \vec{G} t) \cdot \vec{r}}, \quad (1.5)$$

where $\rho(\vec{r})$ is the spin density distribution. In this formula the relaxation effects are neglected and a homogeneous B_0 -field and an ideal gradient linearity are assumed. Consequences of the non ideal case are discussed in the next chapter.

1.1.2 Positron Emission Tomography

As shown in Figure 1.2 the basic principle of PET imaging is the detection and reconstruction of annihilating photon events [23]. The patient is injected with

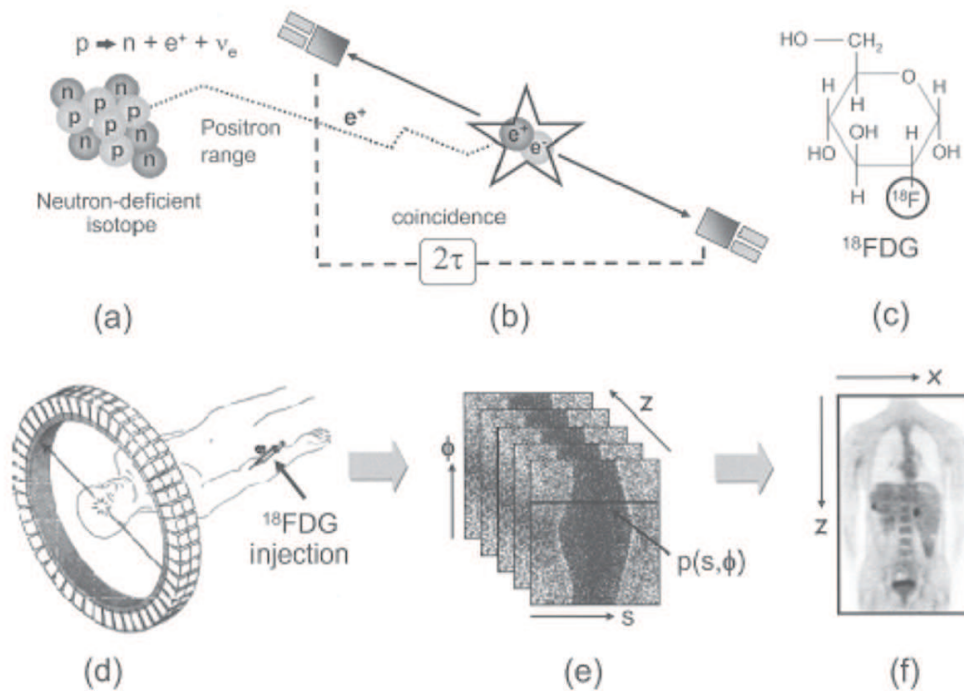


Figure 1.2: Schematic description of the basic principles of PET imaging. In a β^+ -decay a neutron-deficient isotope emits a positron (a). The 2 annihilation photons are detected in coincidence (b). Deoxyglucose labeled with the positron-emitter ^{18}F (c). PET detector ring registers a pair of annihilation photons (d). Positron annihilation events are stored in sinograms where each element of the sinogram contains the number of annihilations in a specific projection direction (e). Reconstructed image (f). Adapted from [23]

a radiotracer, usually deoxyglucose labeled with a positron-emitter ^{18}F . In a β^+ -decay this neutron-deficient isotope emits a positron which then annihilates with an electron. The two annihilation photons are detected in coincidence by the PET detector ring. The coincidence events are grouped into the projection

directions and stored in a sinogram where each element of the sinogram contains the number of annihilations in a specific projection direction. A filtered back projection or iterative expectation-maximization algorithms are used for image reconstruction.

1.1.3 Characteristics of MRI and PET

The combination of PET and MRI combines the advantages of both systems: high sensitivity, high spatial resolution and excellent soft tissue contrast. The latest PET detector offers a very sensitive detection of radioisotopes in the order of picomolar concentrations [24]. MRI provides a spatial resolution in the sub-millimeter range and allows for different tissue contrasts. The complementarity of these characteristics suggests an integrative approach. However, for the interference-free integration of the PET detector in an MRI system several challenges have to be overcome as described in the next section.

1.2 Challenges in MR/PET

MR and PET are complementary in the clinical information they provide, but their physical functionalities usually interfere when operated in close proximity. Without any technical modifications, the MRI magnetic field interferes with the conventional PET detectors that are used in clinical PET/CT systems and that employ photomultiplier tubes (PMT). In the past, several modifications to the PET detector, e.g. connecting light fibers [25] or using avalanche photodiodes (APD) [7, 26], have been discussed and effectually implemented to overcome the interference between the modalities in an integrated system. Figure 1.3 shows the sensitivity of conventional PMT-based PET detectors and APDs to the magnetic field. Figure 1.4 schematically shows the integration of the PET detector in the MR hardware structure.

Besides the hardware integration a new challenge in MR/PET is the attenuation correction of the PET data. This attenuation correction can be performed based on the MR data. However, the MR contrast is independent of the electron density of the tissue and thus contains no direct information of the photon attenuation magnitude. A rough overview of the concepts of MR-based attenuation correction for the hardware and the human tissue is given in the next section. The next chapters provide a more detailed description.

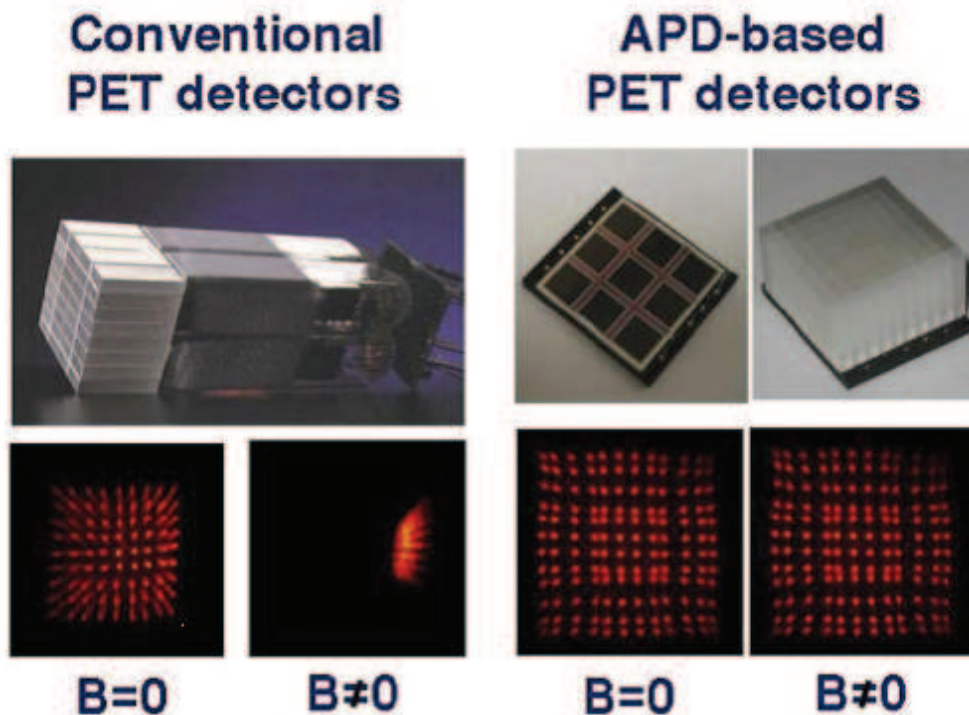


Figure 1.3: Effect of magnetic fields on the readout map of PET detectors. While the conventional PMT-based detectors are highly sensitive to even small magnetic fields, the detector-element map of the APD-based detectors is undistorted even if operating inside a magnetic field of 7T. Adapted from [12].

1.3 MR-based Attenuation Correction

The emitted 511 keV photons may be attenuated on their pathway by either MR equipment, the PET gantry, or the patient's body. Therefore, the PET reconstruction must be corrected for attenuation. The attenuation correction factors

$$ACF = \exp\left(-\int \mu(r)dr\right) \quad (1.6)$$

for the PET emission data are computed as the line of integrals of 511 keV photon attenuation μ along each line of response of the PET detector [27]. In contrast to a PET/CT system where the attenuation-coefficient data are generated by converting the CT images to an attenuation map at 511 keV, in MR/PET the attenuation map and the corresponding attenuation correction are more challenging to generate. The MR hardware inside the PET field-of-view (FoV), particularly the surface coils and the patient table, can be manufactured of less attenuating components, or, preferably, attenuating components can be placed outside the PET FoV. The attenuation correction of residual hardware

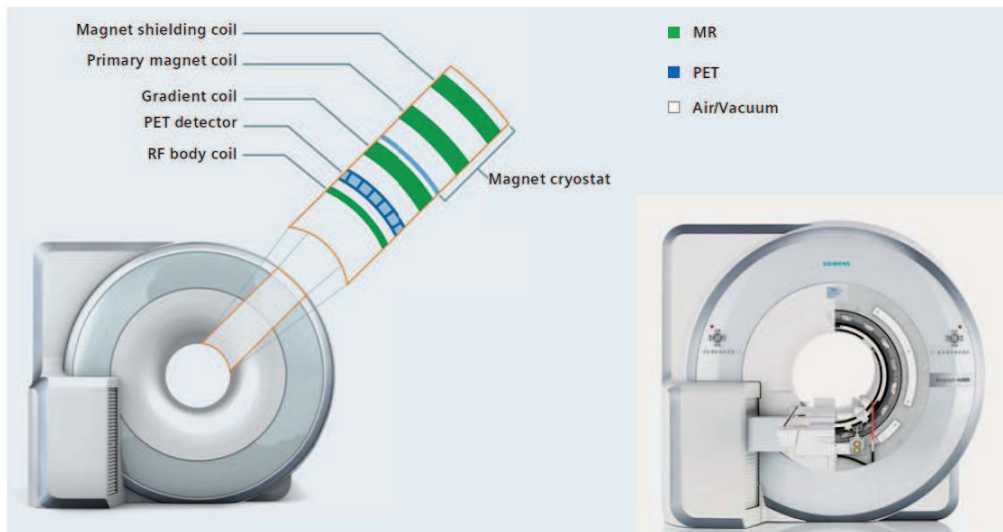


Figure 1.4: Integrated whole-body MR/PET system showing the integration of the PET detectors in the MR hardware structure. From inside to outside: RF body coil, PET detector, gradient coil assembly, primary magnet coil, and magnet shielding coil. Adapted from [14].

can be performed by considering the position and the attenuation coefficients of each hardware component [28].

For the human attenuation correction new concepts are required. Several approaches are available for generating an attenuation map from an MR image [29–34]. Segmentation in different body compartments [34] and an atlas registration approach [33] have been proposed. Figure 1.5 shows the PET reconstruction before and after the performed human attenuation correction.

MR information containing the whole patient anatomy within the visible PET FoV is required to perform an unbiased human attenuation correction. However, the MR-based field-of-view (FoV) is limited due to physical restrictions such as inhomogeneity of the main magnetic field and nonlinearity of the gradient field [35–40]. This FoV limitation causes truncations in the MR-based attenuation correction map and might hamper an accurate attenuation correction in MR/PET hybrid imaging [41]. The impact on the FoV limitation is shown in Figure 1.6.

1.4 MR-based FoV Extension

In conventional MR Fourier transform imaging, a proper spatial encoding requires a homogeneous main magnetic field and linear gradient fields. These conditions are fulfilled for typical FoV volumes at iso-center positions. At off-center

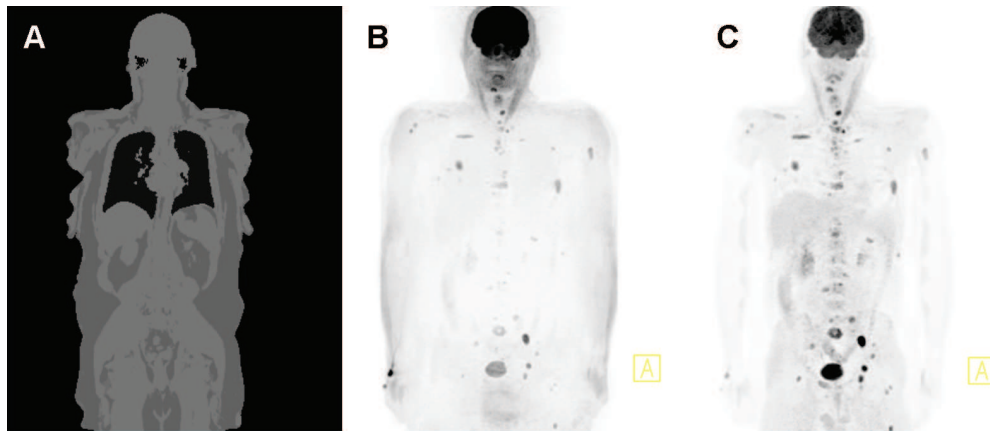


Figure 1.5: Human attenuation correction. Two-point Dixon-based attenuation correction map segmented in soft-tissue, fat, lung-tissue and background (A). Maximum intensity projection (MIP) of PET reconstruction without (B) and with attenuation correction (C). Note the improved visibility of lesions in C.

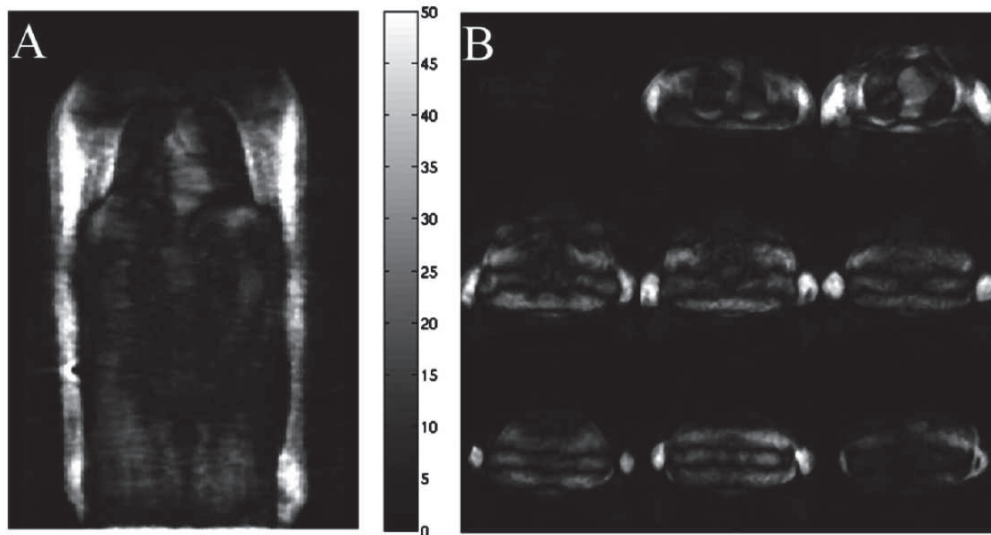


Figure 1.6: Reconstruction bias due to FoV limitation in attenuation correction expressed as percentile deviation from the correct uptake. Adapted from [41].

positions, inhomogeneities of the main magnetic field and gradient nonlinearities cause geometrical distortions of body regions located outside the specified FoV, such as the patient's arms [37, 38, 42]. Typical truncations of the patient's arms are shown in Fig. 1.5A. However, the distortion due to the inhomogeneity of the main magnetic field scales with the applied gradient strength, whereas the distortion due to the gradient nonlinearity is constant [35, 39]. In this thesis it is shown that an optimal gradient strength can be found to compensate the distortion due to the described field imperfections.

1.5 Aim and Outline of this Thesis

In this thesis a new method for MR-based FoV extension is described. The distortion due to the inhomogeneity of the main magnetic field is compensated by the distortion due to the nonlinearity of the gradient field using an optimal gradient amplitude. The dependency of geometrical distortions on the applied gradient strength is analyzed in simulations and phantom measurements. After validation of the proposed method, various implementations are developed aiming at a reduction of the measurement time and an optimization of the workflow. Finally, the impact of the new imaging technique is shown for 12 patients.

In **chapter 2** a detailed analysis of the hardware-dependent causes of FoV limitations is performed. The inhomogeneity of the main magnetic field and the nonlinearity of the gradient field are characterized and the influence of the spatial encoding is discussed. The proposed extended FoV imaging technique is introduced in **chapter 3**. The improvement is validated in simulations and phantom measurements. **Chapter 4** describes three different implementations of the FoV extending method. Firstly, a multislice spin-echo-based sequence is developed to allow for the optimal gradient amplitude for each slice position. Secondly, a dual-echo spin-echo-based sequence is implemented to reduce the distortion of both patient's arms in the same radio-frequency (RF) excitation train. Thirdly, the proposed transaxial FoV extension method is combined with a continuous table move technique to achieve an additional extended FoV coverage also in axial direction. Finally, in **chapter 5** the impact of the proposed acquisition technique on the PET quantification is shown in a patient study.

References

- [1] Mansfield P, Grannell PK. NMR 'diffraction' in solids? *J. Phys. C: Solid State Phys.* 1973;6(22):L422–L426.
- [2] Lauterbur PC. Image Formation by Induced Local Interactions: Examples Employing Nuclear Magnetic Resonance. *Nature* 1973;242:190–191.

- [3] Delso G, Furst S, Jakoby B, Ladebeck R, Ganter C, Nekolla SG, Schwaiger M, Ziegler SI. Performance measurements of the Siemens mMR integrated whole-body PET/MR scanner. *J. Nucl. Med.* 2011;52(12):1914–1922.
- [4] Schlemmer HP, Pichler BJ, Krieg R, Heiss WD. An integrated MR/PET system: prospective applications. *Abdom Imaging* 2009;34:668–674.
- [5] Herzog H, Pietrzyk U, Shah NJ, Ziemons K. The current state, challenges and perspectives of MR-PET. *Neuroimage* 2010;49:2072–2082.
- [6] Beyer T, Pichler B. A decade of combined imaging: from a PET attached to a CT to a PET inside an MR. *Eur. J. Nucl. Med. Mol. Imaging* 2009;36 Suppl 1:1–2.
- [7] Wehrl HF, Judenhofer MS, Thielscher A, Martirosian P, Schick F, Pichler BJ. Assessment of MR compatibility of a PET insert developed for simultaneous multiparametric PET/MR imaging on an animal system operating at 7 T. *Magn Reson Med* 2011;65:269–279.
- [8] Wehrl HF, Sauter AW, Judenhofer MS, Pichler BJ. Combined PET/MR imaging—technology and applications. *Technol. Cancer Res. Treat.* 2010;9:5–20.
- [9] Catana C, Procissi D, Wu Y, Judenhofer MS, Qi J, Pichler BJ, Jacobs RE, Cherry SR. Simultaneous in vivo positron emission tomography and magnetic resonance imaging. *Proc. Natl. Acad. Sci. U.S.A.* 2008;105:3705–3710.
- [10] Catana C, Wu Y, Judenhofer MS, Qi J, Pichler BJ, Cherry SR. Simultaneous acquisition of multislice PET and MR images: initial results with a MR-compatible PET scanner. *J. Nucl. Med.* 2006;47:1968–1976.
- [11] Pichler BJ, Kolb A, Nagele T, Schlemmer HP. PET/MRI: paving the way for the next generation of clinical multimodality imaging applications. *J. Nucl. Med.* 2010;51:333–336.
- [12] Pichler BJ, Wehrl HF, Kolb A, Judenhofer MS. Positron emission tomography/magnetic resonance imaging: the next generation of multimodality imaging? *Semin Nucl Med* 2008;38:199–208.
- [13] Pichler BJ, Judenhofer MS, Wehrl HF. PET/MRI hybrid imaging: devices and initial results. *Eur Radiol* 2008;18:1077–1086.
- [14] Quick HH, Ladebeck R, Georgi JC. Whole-Body MR/PET Hybrid Imaging: Technical Considerations, Clinical Workflow, and Initial Results. *Magn Tom FLASH* 2011;46:88–100.
- [15] Schwenzer NF, Schmidt H, Claussen CD. Whole-body MR/PET: applications in abdominal imaging. *Abdom Imaging* 2012;37(1):20–28.

- [16] Bisdas S, Nagele T, Schlemmer HP, Boss A, Claussen CD, Pichler B, Ernemann U. Switching on the lights for real-time multimodality tumor neuroimaging: The integrated positron-emission tomography/MR imaging system. *AJNR Am J Neuroradiol* 2010;31:610–614.
- [17] Boss A, Bisdas S, Kolb A, Hofmann M, Ernemann U, Claussen CD, Pfannenbergl C, Pichler BJ, Reimold M, Stegger L. Hybrid PET/MRI of intracranial masses: initial experiences and comparison to PET/CT. *J. Nucl. Med.* 2010;51:1198–1205.
- [18] Boss A, Kolb A, Hofmann M, Bisdas S, Nagele T, Ernemann U, Stegger L, Rossi C, Schlemmer HP, Pfannenbergl C, Reimold M, Claussen CD, Pichler BJ, Klose U. Diffusion tensor imaging in a human PET/MR hybrid system. *Invest Radiol* 2010;45:270–274.
- [19] Bouchelouche K, Turkbey B, Choyke P, Capala J. Imaging prostate cancer: an update on positron emission tomography and magnetic resonance imaging. *Curr Urol Rep* 2010;11:180–190.
- [20] Buscher K, Judenhofer MS, Kuhlmann MT, Hermann S, Wehrl HF, Schafers KP, Schafers M, Pichler BJ, Stegger L. Isochronous assessment of cardiac metabolism and function in mice using hybrid PET/MRI. *J. Nucl. Med.* 2010;51:1277–1284.
- [21] Nekolla S, Souvatzoglou M, Schachoff S, Fuerst S, Martinez-Moeller A, Ziegler S, Schwaiger M. MR/PET Attenuation correction using a multi tissue model for quantification of cardiac uptake: Initial comparison to PET/CT. *J Nucl Med* 2011;52 Suppl 1:440.
- [22] Drzezga A, Souvatzoglou M, Eiber M, Beer AJ, Fuerst S, Martinez-Moeller A, Nekolla SG, Ziegler S, Ganter C, Rummeny EJ, Schwaiger M. First Clinical Experience with Integrated Whole-Body PET/MR: Comparison to PET/CT in Patients with Oncologic Diagnoses. *J. Nucl. Med.* 2012;53(6):845–855.
- [23] Townsend DW. Physical principles and technology of clinical PET imaging. *Ann. Acad. Med. Singap.* 2004;33(2):133–145.
- [24] Grupen C and Buvat I. *Handbook of Particle Detection and Imaging.* Springer; 2012.
- [25] Shao Y, Cherry SR, Farahani K, Slates R, Silverman RW, Meadors K, Bowery A, Siegel S, Marsden PK, Garlick PB. Development of a PET detector system compatible with MRI/NMR systems. *IEEE Trans NuclearSci* 1997;44:1167–1171.
- [26] Pichler BJ, Judenhofer MS, Catana C, Walton JH, Kneilling M, Nutt RE, Siegel SB, Claussen CD, Cherry SR. Performance test of an LSO-APD

- detector in a 7-T MRI scanner for simultaneous PET/MRI. *J. Nucl. Med.* 2006;47:639–647.
- [27] Bailey DL and Townsend DW and Valk PE and Maisey MN. *Positron emission tomography: basic sciences.* Springer; 2005.
- [28] Delso G, Martinez-Moeller A, Bundschuh RA, Ladebeck R, Candidus Y, Faul D, Ziegler SI. Evaluation of the attenuation properties of MR equipment for its use in a whole-body PET/MR scanner. *Phys Med Biol* 2010;55:4361–4374.
- [29] Hofmann M, Pichler B, Scholkopf B, Beyer T. Towards quantitative PET/MRI: a review of MR-based attenuation correction techniques. *Eur. J. Nucl. Med. Mol. Imaging* 2009;36 Suppl 1:93–104.
- [30] Kops RE, Herzog H. Alternative methods for attenuation correction for PET images in MR-PET scanners. *Nuclear Science Symposium Conference Record, 2007. NSS '07. IEEE.* Vol. 6. p. 4327-4330.
- [31] Beyer T, Weigert M, Quick HH, Pietrzyk U, Vogt F, Palm C, Antoch G, Muller SP, Bockisch A. MR-based attenuation correction for torso-PET/MR imaging: pitfalls in mapping MR to CT data. *Eur. J. Nucl. Med. Mol. Imaging* 2008;35(6):1142–1146.
- [32] Martinez-Moeller A, Souvatzoglou M, Delso G, Bundschuh RA, Chefd'hotel C, Ziegler SI, Navab N, Schwaiger M, Nekolla SG. Tissue classification as a potential approach for attenuation correction in whole-body PET/MRI: evaluation with PET/CT data. *J. Nucl. Med.* 2009;50(4):520–526.
- [33] Hofmann M, Steinke F, Scheel V, Charpiat G, Farquhar J, Aschoff P, Brady M, Scholkopf B, Pichler BJ. MRI-based attenuation correction for PET/MRI: a novel approach combining pattern recognition and atlas registration. *J. Nucl. Med.* 2008;49:1875–1883.
- [34] Le Goff-Rougetet R and Frouin V and Mangin J-F and Bendriem B. Segmented MR images for brain attenuation correction in PET. In *Proceedings of the SPIE 2167, 1994*, p. 725.
- [35] Bakker CJ, Moerland MA, Bhagwandien R, Beersma R. Analysis of machine-dependent and object-induced geometric distortion in 2DFT MR imaging. *Magn Reson Imaging* 1992;10:597–608.
- [36] Wald L, Schmitt F, Dale A. Systematic Spatial Distortion in MRI due to Gradient Non-Linearities. *NeuroImage* 2001;13(6):50.
- [37] Dammann P, Kraff O, Wrede KH, Ozkan N, Orzada S, Mueller OM, Sandalcioğlu IE, Sure U, Gizewski ER, Ladd ME, Gasser T. Evaluation of hardware-related geometrical distortion in structural MRI at 7 Tesla for

- image-guided applications in neurosurgery. *Acad Radiol* 2011;18(7):910–916.
- [38] Wang D, Strugnell W, Cowin G, Doddrell DM, Slaughter R. Geometric distortion in clinical MRI systems Part I: evaluation using a 3D phantom. *Magn Reson Imaging* 2004;22(9):1211–1221.
- [39] Michiels J, Bosmans H, Pelgrims P, Vandermeulen D, Gybels J, Marchal G, Suetens P. On the problem of geometric distortion in magnetic resonance images for stereotactic neurosurgery. *Magn Reson Imaging* 1994;12:749–765.
- [40] Stanescu T, Jans HS, Wachowicz K, Fallone BG. Investigation of a 3D system distortion correction method for MR images. *J Appl Clin Med Phys* 2010;11(1):2961.
- [41] Delso G, Martinez-Moeller A, Bundschuh RA, Nekolla SG, Ziegler SI. The effect of limited MR field of view in MR/PET attenuation correction. *Med Phys* 2010;37:2804–2812.
- [42] Baldwin LN, Wachowicz K, Thomas SD, Rivest R, Fallone BG. Characterization, prediction, and correction of geometric distortion in 3 T MR images. *Med Phys* 2007;34:388–399.

Chapter 2

Analysis of Hardware-Dependent Geometrical Distortion

Parts of this chapter have been submitted:

Blumhagen JO, Ladebeck R, Fenchel M, Scheffler K. MR-based field-of-view Extension in MR/PET: B_0 Homogenization Using Gradient Enhancement. *Magnetic Resonance in Medicine 2012, in print.*

2.1 Introduction

In MRI, it is well known that a precise spatial-encoding is inherently limited by the B_0 inhomogeneity of the main magnetic field and the nonlinearity of the gradient field. Particularly for large FoVs, the MR image is prone to hardware-related geometrical distortions [1–6]. However, several applications such as an MR-based attenuation correction or an MR-based radiotherapy treatment planning are of growing interest and require methods for sufficient image fidelity also for very large FoVs [7]. In this chapter, the distortion is analyzed in terms of an FoV extension even at regions of interest outside the specified FoV.

The standard approach of distortion reduction is the use of very strong gradients and an applied post-processing gradient distortion correction. Strong gradients reduce the distortions due to B_0 inhomogeneity as derived in detail in the next section. The nonlinearity of the gradient field is known from the design and can thus be used for a post-processing correction of that part of the distortion, which is due to the nonlinearity. However, while this is feasible within the specified FoV, it might fail outside the specified FoV (radius $|r| > 25$ cm from iso-center). Here, the gradient slope decreases drastically and might even be inverted so that pixels at different positions are encoded with the same frequency. Hence, a post-processing correction is not feasible anymore as shown in the results section of this chapter.

Many approaches of distortion reduction within the specific FoV have been proposed [8–16]. Several methods are based on single point acquisition techniques including a refocusing pulse for each point in k-space [17–19]. In terms of specific absorption rate (SAR), these techniques are not well applicable for human imaging [20]. Cho et al. investigated the correction of B_0 including chemical shifts and susceptibility using a so called view-angle-tilting technique [21]. A gradient in slice-select direction was added simultaneously to the readout gradient, producing a tilted slice, which corrected the field inhomogeneity dependent geometrical distortion. The patent of the same author describes an imaging technique in fringe fields requiring full phase encoding in the x- and y-direction [22]. A method in the presence of a static field with a permanent gradient was proposed by Epstein et al. [20]. This so called slant-slice imaging technique acquires entire lines of k-space with each readout and features low-SAR. Chang and Fitzpatrick developed a very simple method of distortion reduction due to B_0 inhomogeneities [14]. This gradient-reversal technique requires two identical acquisitions except for the polarity of the readout gradient. An extension of the view-angle-tilting with an additional z-phase encoding was presented by Lu et al. [23]. This technique was successfully used for imaging in the presence of metal-induced field inhomogeneities and was thus called Slice Encoding for Metal Artifact Correction (SEMAC). While the view-angle-tilting reduces the in-plane distortions, the z-phase encoding eliminates the through-plane distortion.

Although the presented methods achieved interesting results in distortion reduction due to B_0 inhomogeneities, none of these techniques aimed a correction of the strong distortions due to the gradient nonlinearities outside the specified FoV. Langlois et al. demonstrated a simple approach to correct the gradient nonlinearities within a FoV of up to 384 mm [15]. In this chapter, we will analyze the distortion due to both the B_0 inhomogeneities and the gradient nonlinearities. These analyses were not limited to the specified FoV but also included regions outside the usual specified FoV (diameter > 500 mm). A novel compensation method of both error sources allowing a significant FoV extension of up to 600 mm in diameter is proposed in the following chapter 3.

2.2 Theory

In the absence of any B_0 field inhomogeneity and gradient nonlinearity effects, the received signal S can be represented in 3D-Fourier-transform NMR:

$$S(\vec{k}) = \int d^3r \rho(\vec{r}) e^{i2\pi(\vec{k} \cdot \vec{r})}, \quad (2.1)$$

where $\rho(\vec{r})$ is the spin density distribution and $\vec{k} = \frac{1}{2\pi}\gamma\vec{G}t$ is the k-vector. The Fourier-transform (FT) assumes a homogeneous main magnetic field and linear gradients. In the non-ideal case, B_0 inhomogeneities and gradient nonlinearities may perturb the spatial encoding. The deviation of actual phase/frequency values from the expected ones leads to distortions in the image space. Taking gradient nonlinearities into account, in 2D Fourier-transform spin echo (SE) imaging the k-vector is modified as follows:

$$\vec{k}_{x,y} = \frac{1}{2\pi}\gamma\vec{G}t_{x,y} \Rightarrow \vec{k}_{x,y} = \frac{1}{2\pi}\gamma(\vec{G} + \Delta\vec{G})t_{x,y}, \quad (2.2)$$

where γ is the gyromagnetic ratio, \vec{G} is the ideal gradient vector, $\Delta\vec{G}$ is the gradient nonlinearity and $t_{x,y} = (TE - t, \tau_y)$ are the gradient-on times for the signal readout t and phase encoding τ .

Assuming the time of the spin echo coincides with the time of the gradient echo [24], the presence of inhomogeneities ΔB_0 in the main magnetic field leads to an additional phase offset by a factor of

$$\phi(t) = \gamma\Delta B_0(TE - t). \quad (2.3)$$

Therefore, the signal in the presence of gradient nonlinearities and inhomogeneities in the main magnetic field is:

$$S(G_x, G_y) = \int_x \int_y \rho(x, y, z_0) e^{-i\gamma(xG_x + x\Delta G_x + \Delta B_0)(TE - t)} e^{-i\gamma(yG_y + y\Delta G_y)\tau_y} dx dy. \quad (2.4)$$

In comparison with the ideal case the pixel will be shifted in the readout direction

$$x' = x + \frac{\Delta B_{G_x}(x, y, z)}{G_x} + \frac{\Delta B_0(x, y, z)}{G_x}, \quad (2.5)$$

in the phase-encoding direction

$$y' = y + \frac{\Delta B_{G_y}(x, y, z)}{G_y}, \quad (2.6)$$

and in the through-plane direction

$$z' = z + \frac{\Delta B_{G_z}(x, y, z)}{G_z} + \frac{\Delta B_0(x, y, z)}{G_z}, \quad (2.7)$$

where x, y, z are the actual positions, x', y', z' are the distorted positions and $\Delta \vec{B}_{\vec{G}} = \Delta \vec{G} \cdot \vec{r}$ is the magnetic field produced by the gradient nonlinearity of $\Delta \vec{G}$ [1, 5]. The distortion in the phase-encoding direction depends only on the gradient nonlinearities, whereas the distortion in the readout direction and in the slice-select direction depends on the gradient nonlinearities and the B_0 inhomogeneities.

2.3 Materials and Methods

2.3.1 Measurements of Magnetic Fields

Measurements of the main magnetic field and the gradient field were performed using a half-moon probe array (Metrolab Instruments SA, Geneva, Switzerland). The probe array (Fig. 2.1) contains 24 NMR probes rotating around the magnetic field axis with 24 angular positions per turn. It was placed at the magnet's iso-center with an accuracy of ± 1 mm. An additional fine adjustment of the probe array's z-position was performed by seeking the intersection point of a positive and a negative applied gradient. An identical iso-center position of the main magnetic field and the gradient coil was assumed. The local field frequencies were measured at 576 positions (24 NMR probes, 24 angular positions) on a sphere's surface of 500 mm in diameter. The gradient field was determined by setting a gradient offset of 1 mT/m and subtracting of the main magnetic field data. The resulting field parameters were stored in spherical harmonics.

2.3.2 Simulation of Distortion

Simulations were performed using Matlab R2010b (The MathWorks, Inc., Natick, MA, USA). The magnetic field values were calculated using spherical har-

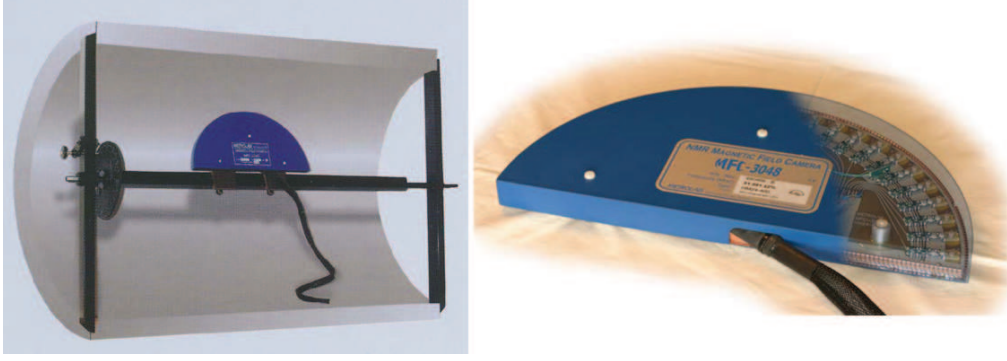


Figure 2.1: Magnetic-field camera consisting of 24 NMR probes. The measurement device is adjusted to the iso-center and placed parallel to the main magnetic field axis. A spherical magnetic field plot can be acquired by rotating around the magnetic field axis in 24 angular positions.

monic expansion from the measured spherical harmonic coefficients:

$$B(r, \theta, \phi) = \sum_{n=0}^{n_{max}} \sum_{m=0}^{n; m \leq 12} \left(\frac{r}{r_0}\right)^n P_{nm}(\cos \theta) [A_{nm} \cos m\phi + B_{nm} \sin m\phi], \quad (2.8)$$

where A_{nm} and B_{nm} are the spherical harmonic coefficients, P_{nm} are the associated Legendre functions and r_0 is the normalization radius [25, 26]. The maximum order of n is $n_{max} = 23$ and the maximum order of m is $m_{max} = 12$. All further simulations were based on these measured field values.

In-plane Distortion

The in-plane distortion in the readout direction was simulated voxel-wise according to Eq. 2.5 for the B_0 inhomogeneity, the gradient nonlinearity, and both. The FoV was set to $x, y = \pm 300$ mm to achieve also quantitative distortion data outside the usual specified FoV. Simulation parameters were: transversal slice at iso-center position ($z = 0$ m), in-plane matrix: $256 * 256$, readout gradient $G_{RO} = 5$ mT/m.

For a specific position outside the usual specified FoV ($x = -0.284$ m, $y = 0.028$ m, $z = 0$ m) the distortion in readout direction was simulated for different readout gradient amplitudes $G_{RO} = [\pm 1.03$ mT/m, ± 1.56 mT/m, ± 2.12 mT/m, ± 3.31 mT/m, ± 4.52 mT/m, ± 5.72 mT/m, ± 6.90 mT/m, ± 8.09 mT/m, 9.39 mT/m].

Through-plane Distortion and Slice Profile

The through-plane distortion was simulated according to Eq. 2.7 due to both the B_0 inhomogeneity and the nonlinearity of the slice-select gradient. Simulation parameters were: transversal slice at iso-center position ($z=0\text{m}$), 5mm thickness, in-plane resolution: $2.0 * 2.0 \text{ mm}^2$, slice-select gradient $G_{SS} = 20 \text{ mT/m}$. The slice profiles of 7 slices ($z=[-0.12 \text{ m}, +0.12 \text{ m}]$, distance of 40 mm, thickness of 5 mm) were simulated in an extremely extended FoV (0.646 m diagonal) using a slice-select gradient of $G_z = 20 \text{ mT/m}$.

2.3.3 Phantom Measurements

Experiments for validating the stated dependency of the in-plane distortion in frequency-encoding direction on the B_0 inhomogeneity and gradient nonlinearity (Eq. 2.5) have been performed using a grid-structure phantom (Fig. 2.2) consisting of spheres of 1 cm in diameter placed on a $2 * 2 * 2 \text{ cm}^3$ grid. A reference



Figure 2.2: Grid-structure phantom consisting of spheres of 1cm in diameter placed on a $2 * 2 * 2 \text{ cm}^3$ grid.

scan of the phantom at the iso-center position and multiple measurements of the phantom shifted in x-direction were performed using the same readout gradient amplitudes as in the simulation. A spin echo sequence was used to acquire a FoV of $500 * 500 \text{ mm}^2$ shifted to an extreme off-center position ($-350 \text{ mm} < x$

< 150 mm, -250 mm $< y < 250$ mm, $z = 0$ mm) with an in-plane matrix of 256×256 , TE = 12 ms, TR = 300 ms, and 5 mm slice thickness. The image positions of the spheres were assigned to the real positions defined by the grid geometry. The determined distortions in readout direction were analyzed and compared to simulations depending on the applied gradient amplitudes.

Experiments for analyzing the through-plane distortion have been performed using a slice-phantom. The dimension of the phantom was $40 \times 6 \times 1$ cm³. To image the distortion in the z-direction the slice-phantom was positioned in the x-,y-direction at $z = 0$ m and coronal slices were acquired. The readout gradient was varied in amplitude and polarity, $G_z = 1.62$ mT/m, $G_z = -1.62$ mT/m, $G_z = 19.56$ mT/m.

2.4 Results

2.4.1 Frequency Mapping

The simulated frequency-encoding is shown one-dimensionally for the x-axis (-30 cm $< x < 30$ cm, $y = 0$ m, $z = 0$ m) in Figure 2.3. Using a strong readout gradient of $G_x = 40$ mT/m the achieved frequency was linear with the x-position within the usual specified FoV but became nonlinear at very off-center positions ($x > 25$ cm). Here, the slope of the gradient decreased significantly with increasing distance from iso-center and was even inverted at position $x = 29$ cm.

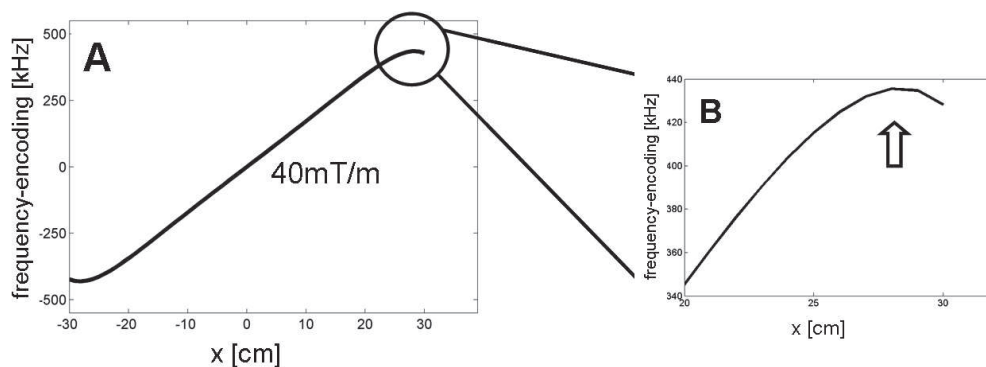


Figure 2.3: Simulation of frequency mapping based on the measured field coefficients. The x-gradient is plotted for an extended range in the x-direction (-30 cm $< x < 30$ cm, $y = 0$ m, $z = 0$ m). While the x-gradient is linear within the specified FoV (A), the slope decreases significantly and is even inverted at an extreme off-center position (B) using the maximum gradient amplitude of 40 mT/m. An injective frequency mapping required for a post-processing distortion correction is not possible.

2.4.2 In-plane Distortion

The pixel-wise simulation of the in-plane distortion in the readout direction is shown in Fig. 2.4. The transversal slice was analyzed at the iso-center position

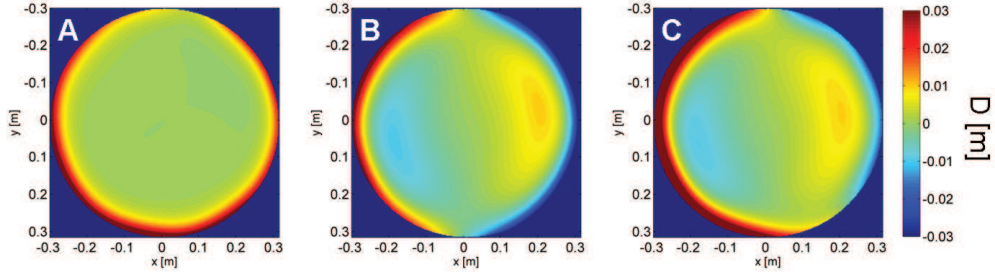


Figure 2.4: In-plane distortion in the readout direction $D[m]$ due to B_0 inhomogeneity (A), gradient nonlinearity (B) and both (C). Transversal slice at iso-center position ($z = 0$ m), in-plane matrix: $256 * 256$, readout gradient $G_{RO} = 5$ mT/m. The readout direction was set to the x-axis.

($z = 0$ m) for an extended FoV of up to 300 mm in transaxial direction. The distortion due to the B_0 inhomogeneity (Fig. 2.4A) and the gradient nonlinearity (Fig. 2.4B) caused a total distortion as shown in Figure 2.4C due to both hardware-related effects. While the distortion within the usual specified FoV is rather small, the distortion due to the B_0 inhomogeneity and the gradient nonlinearity is significantly larger at very off-center positions $|x| > 25$ cm. The B_0 inhomogeneity caused a pixel distortion to the same direction for both the left off-center position ($|x| < 25$ cm) and the right off-center position ($|x| > 25$ cm). The gradient nonlinearity caused a pixel distortion toward iso-center for both the left and the right off-center position. Thus, the total distortion which can be expressed as superimposition of both field errors causes showed a significantly larger distortion for the right off-center position than for the left off-center position.

To validate the simulation results, the in-plane distortion was measured using the grid-structure phantom. Figure 2.5 shows transversal slices of the phantom placed at both iso-center (A) and off-center positions (B, C). The deviation from the assumed actual grid structure is indicated with green vectors from the assumed position to the distorted position for each sphere. The distortion of each sphere was quantified relative to the sphere closest to the iso-center (red marked sphere: undistorted reference position). While the mean distortion of all spheres of the phantom placed at iso-center (Fig. 2.5A) was below 1 mm, there was a significant distortion at very off-center positions. Using a readout gradient strength of $G_x = -8.09$ mT/m (Fig. 2.5B) the maximum distortion of $D_{RO} = 19$ mm was observed at position ($x = -284$ mm, $y = 28$ mm, $z = 0$ m). At the same position the distortion was reduced to $D_{RO} = 6$ mm using a

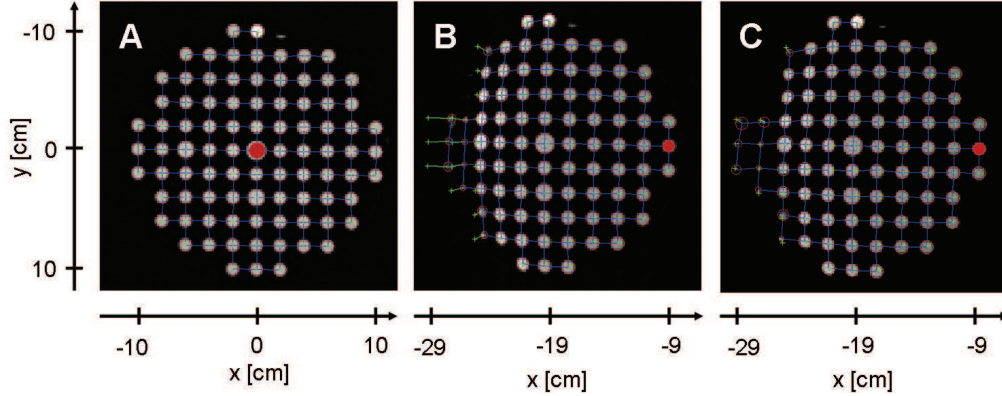


Figure 2.5: Transversal slices of grid-structure phantom. While the reference scan at iso-center position showed very small distortions below $D_{RO} = 1$ mm (A), the observed distortions were more prominent for measurements at very off-center positions of up to 286 mm distant from iso-center (B, C). The magnitude of distortion in readout direction using a readout gradient amplitude of $G_{RO} = -8.09$ mT/m (B) differed significantly from the distortion using a gradient amplitude of $G_{RO} = -2.12$ mT/m (C). Readout direction was left to right. Note the different magnitude of in-plane distortion.

readout gradient amplitude of $G_x = -2.12$ mT/m (Fig. 2.5C).

The measured magnitude of distortion as a function of distance from the iso-center is shown in Figure 2.6 for different readout gradient amplitudes. While the distortions were rather small at positions close to the iso-center, the distortions increased with a strong dependency on the applied readout gradient amplitude for regions outside the usual specified FoV ($x > 25$ cm). The largest measured distortion at position ($x = -284$ mm, $y = 28$ mm, $z = 0$ m) was $D_{RO} = 28$ mm using a readout gradient amplitude of $G_x = 9.39$ mT/m and $D_{RO} = 6$ mm using a readout gradient amplitude of $G_x = -2.12$ mT/m.

Figure 2.7 shows both the simulated and the measured distortion at position ($x = -0.284$ m, $y = 0.028$ m, $z = 0$ m). Stepping through the readout gradient amplitudes changed the magnitude and the direction of distortion. The measured dependency of the gradient amplitude on the distortion was in good agreement with the simulation data, taking usual errors of B_0 - and gradient field measurements into account.

2.4.3 Through-plane Distortion

In the slice-select direction the B_0 inhomogeneity and the gradient nonlinearity of the slice-select gradient cause a through-plane distortion as simulated in Fig-

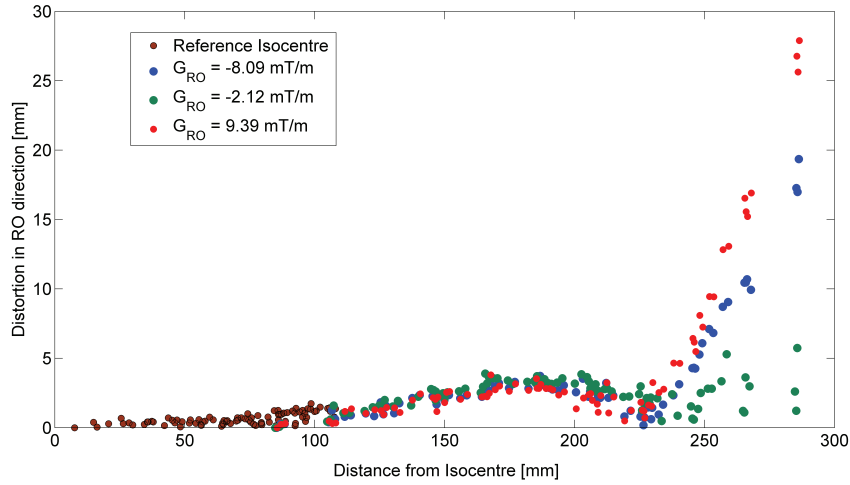


Figure 2.6: Measured distortion in readout direction versus distance from isocenter. The distortion was measured using the grid-structure phantom placed at iso-center position (brown markers) and at extreme off-center positions of up to 30 cm in the x-direction for three different readout gradient amplitudes, $G_{RO} = -8.09$ mT/m (blue markers), $G_{RO} = -2.12$ mT/m (green markers), and $G_{RO} = 9.39$ mT/m (red markers). While the reference measurement at isocenter showed no significant distortion, the measured distortion increased with increasing distance from iso-center. Note also the dependency on the readout gradient strength.

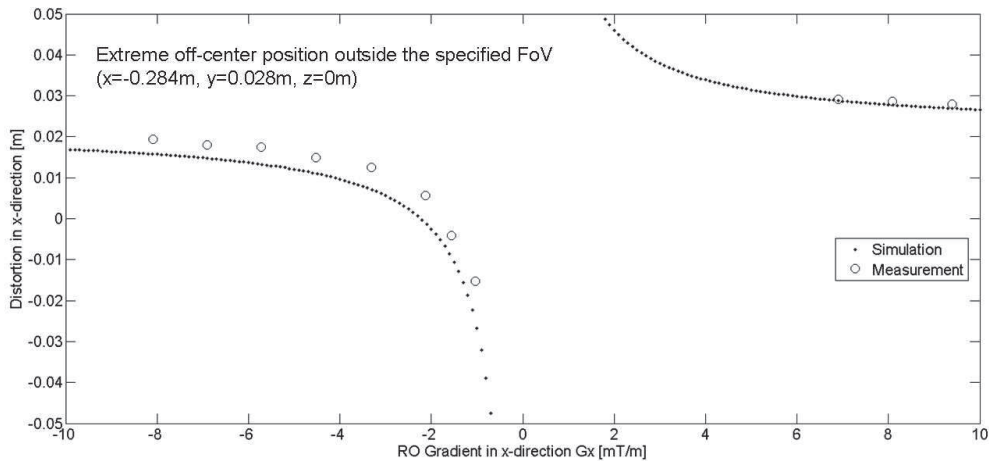


Figure 2.7: In-plane distortion in readout direction versus applied readout gradient at extreme off-center position ($x = -0.284$ m, $y = 0.028$ m, $z = 0$ m). Pixel distortion in simulation data (\bullet) and in phantom measurement (\circ) are shown. There was no post-processing distortion correction applied.

ure 2.8. While no through-plane distortion was observed at iso-center position,

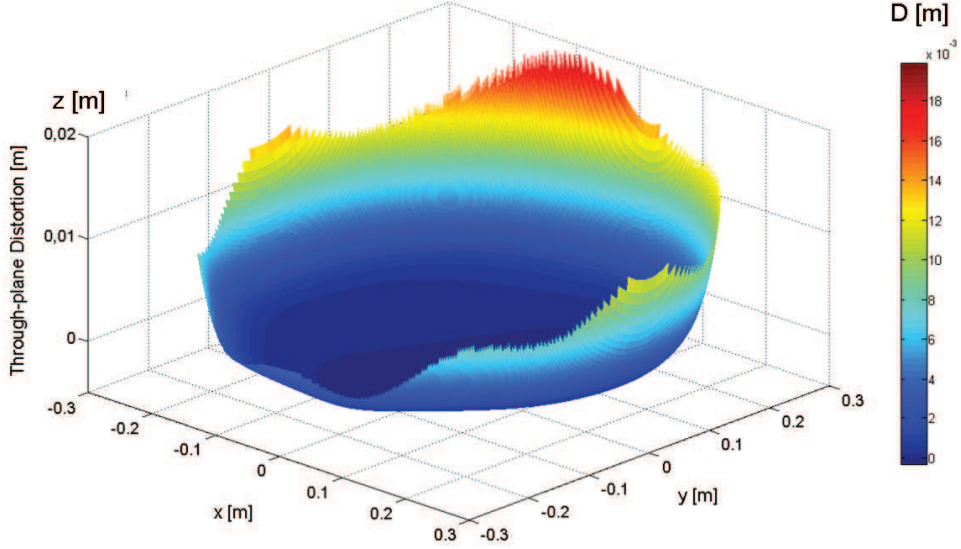


Figure 2.8: Simulation of through-plane distortion using a slice-select gradient of $G_z = 20$ mT/m. Transversal slice at $z = 0$ position was distorted in the slice direction outside the usual specified FoV.

the slice shape tended warping with distance from iso-center and was significantly warped out of slice at very off-center positions ($|x| > 25$ cm) outside the usual FoV. However, the observed magnitude of simulated through-plane distortion was dependent on the off-center position. Using a slice-select gradient of $G_z = 20$ mT/m the absolute value of through-plane distortion $|D|$ was below 5 mm at position ($x = 0$ m, $y = -300$ mm, $z = 0$ m), above 12 mm at positions ($x = [-300$ mm, 300 mm], $y = 0$ m, $z = 0$ m) and up to 18 mm at positions ($y > 250$ mm).

The second effect of B_0 inhomogeneity and gradient nonlinearity on the slice excitation was the change in slice thickness. In Figure 2.9 slice profiles of 5 mm thickness were simulated at positions $z = (-0.12$ m, -0.08 m, -0.04 m, 0 m, $+0.04$ m, $+0.08$ m, $+0.12$ m) in an extremely extended FoV (0.646 m diagonal). While the slice thickness is identical to the nominal value at iso-center position, the slice thickness changed at very off-center positions and depended on the slice position. Using a slice-select gradient of $G_z = 20$ mT/m, a decrease in slice thickness was observed additionally to the through-plane distortions at all simulated slice positions.

In the slice-phantom experiment, distortions in the z -direction were observed. The readout direction was set to the z -direction to visualize the expected through-

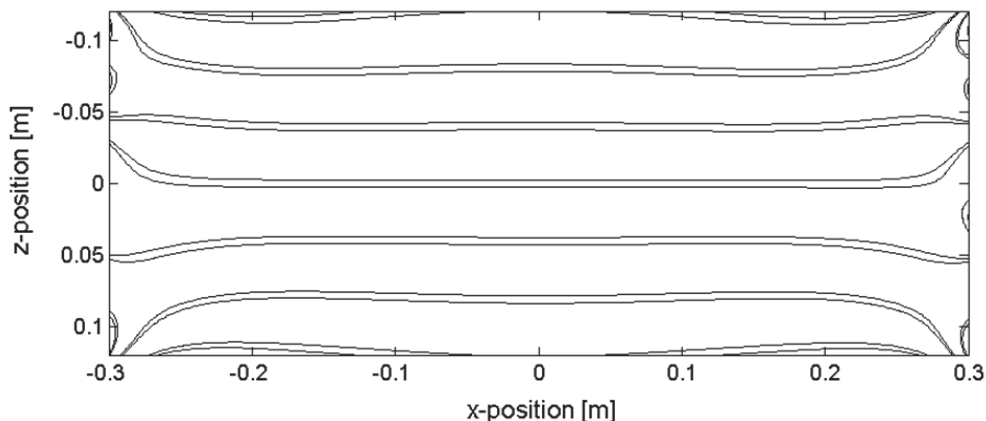


Figure 2.9: Simulation of slice profiles using a slice-select gradient of $G_z = 20$ mT/m. Excitation frequencies and bandwidth were set to simulate slice profiles of 5 mm thickness at positions $z = (-0.12$ m, -0.08 m, -0.04 m, 0 m, $+0.04$ m, $+0.08$ m, $+0.12$ m) in an extremely extended FoV (0.646 m diagonal).

plane distortion of a transversal plane. Figure 2.10 shows these distortions for different gradient amplitudes. While the distortion in the z -direction was small within the usual specified FoV, the distortion increased with increasing distance from iso-center. Furthermore, the polarity of the distortion changed by changing the direction of the gradient amplitude from $G_z = 1.62$ mT/m (Fig. 2.10A) to $G_z = -1.62$ mT/m (Fig. 2.10B). Using a large gradient amplitude of $G_z = 19.56$ mT/m, the distortion was reduced (Fig. 2.10C). In addition, a distortion of constant magnitude was observed in the x -direction (phase-encoding).

2.5 Discussion

The hardware-dependent distortions were observed to be prominent outside the usual specified FoV. While the distortions within the specified FoV appeared to be rather small (mm) and can be corrected in post-processing, the distortions increased significantly (cm) outside the specified FoV. In those regions, the gradient slope might decrease drastically and might even be inverted so that several pixels at different positions are encoded by the same frequency. Therefore, a post-processing distortion correction might fail.

The results of the phantom measurements are in good agreement with those obtained from simulations. Thus, the distortion outside the specified FoV can mainly be described by the B_0 inhomogeneities and the gradient nonlinearities. However, for an accurate description of the distortion behavior, object-related distortions such as object-induced B_0 inhomogeneities at tissue-air interfaces

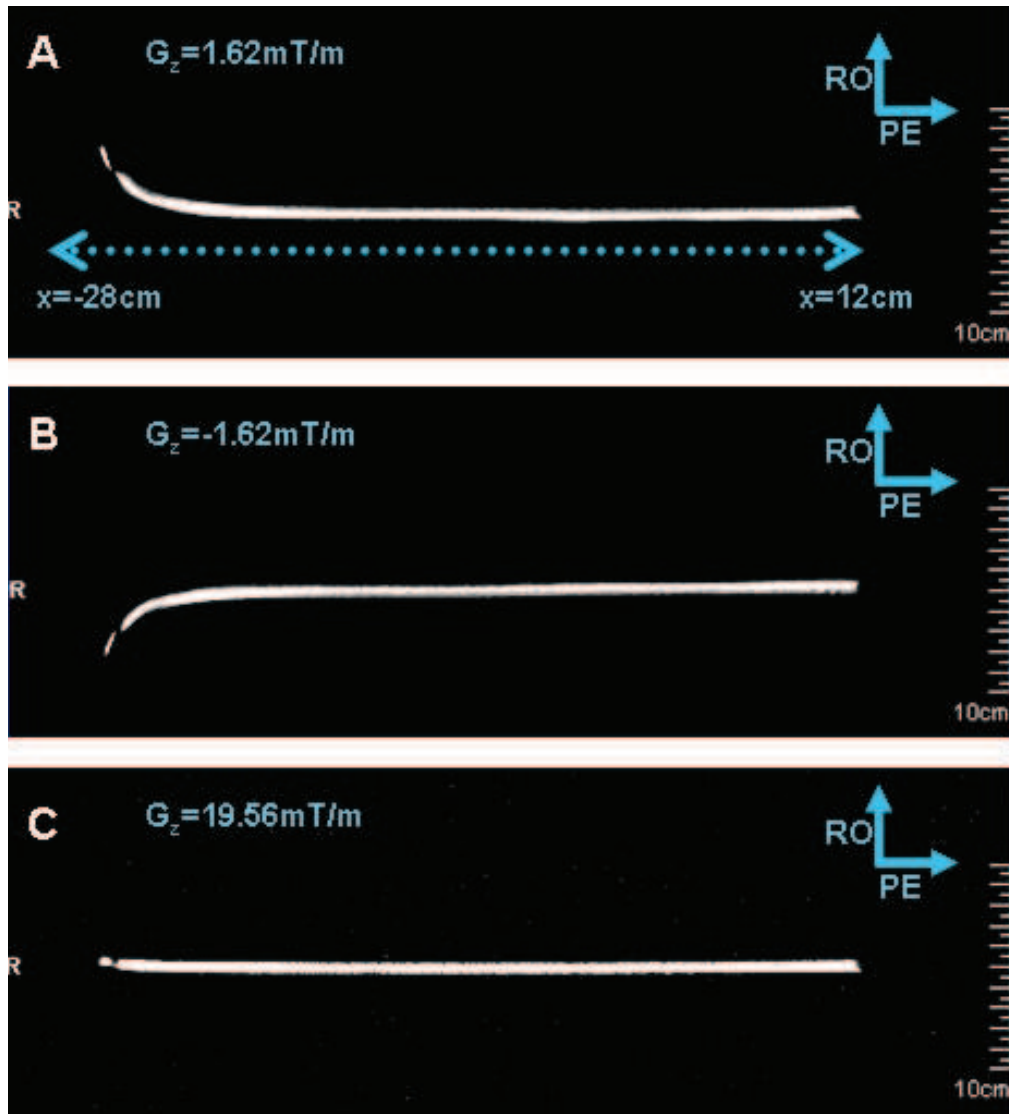


Figure 2.10: Measurement of through-plane distortion. Coronal slices of a slice phantom, which was positioned in the x - y -plane at $z=0\text{m}$, were acquired with readout in the z -direction. The readout gradient was varied in amplitude and polarity, $G_z = 1.62 \text{ mT/m}$ (A), $G_z = -1.62 \text{ mT/m}$ (B), $G_z = 19.56 \text{ mT/m}$ (C). Note the different distortion behavior in the z -direction dependent on the readout gradient amplitude and polarity.

have to be taken into account [1]. In this thesis, the analysis and the correction were focused on the object-induced distortions.

In the slice-select direction the observed out of plane warping and the varying slice thickness are known as *potato chip effect* and *bow-tie effect*, respectively [27–29]. Both effects increased with increasing distance from iso-center. Typical truncation artifacts due to the FoV limitations occur in the patient’s arms. However, in a first order approximation the patient’s arms can be assumed to be homogeneous in the axial direction. Therefore, in this thesis the focus lies on the reduction of the in-plane distortion.

The in-plane distortion was dependent on the position and the readout gradient amplitude with pixel shifts from 0mm to more than 30 mm at very off-center positions outside the usual specified FoV. Both the through-plane distortion and the scanner-induced in-plane distortion in the readout direction were the superimposition of the distortion due to the B_0 inhomogeneity and the gradient nonlinearity. The distortion due to gradient nonlinearities was independent on the gradient amplitude. The distortions due to B_0 inhomogeneities scaled inversely proportional with the gradient amplitude. Thus, with increasing gradient amplitude, the magnitude of the total distortion tended asymptotically to the one caused by the gradient nonlinearity. For very small gradient amplitudes the total distortion increased due to the dominating influence of the B_0 inhomogeneity. However, an optimal gradient amplitude corresponding to zero-distortion was found even at very off-center positions outside the specified FoV. In the following chapter 3, a compensation method of the distortion due to the B_0 inhomogeneity and the distortion due to the gradient nonlinearities is proposed using an optimal gradient amplitude.

2.6 Conclusion

Strong distortions might hamper a faithful spatial encoding at typical positions of the patient’s arms. However, the magnitude of the distortion in frequency-encoding direction is dependent on the readout gradient. Thus, an optimal gradient amplitude can be found to achieve minimal distortion. A detailed analysis of the feasibility of distortion reduction using an optimal space-dependent gradient amplitude is presented in the following chapter.

References

- [1] Bakker CJ, Moerland MA, Bhagwandien R, Beersma R. Analysis of machine-dependent and object-induced geometric distortion in 2DFT MR imaging. *Magn Reson Imaging* 1992;10:597–608.

- [2] Wald L, Schmitt F, Dale A. Systematic Spatial Distortion in MRI due to Gradient Non-Linearities. *NeuroImage* 2001;13(6):50.
- [3] Dammann P, Kraff O, Wrede KH, Ozkan N, Orzada S, Mueller OM, Sandalcioglu IE, Sure U, Gizewski ER, Ladd ME, Gasser T. Evaluation of hardware-related geometrical distortion in structural MRI at 7 Tesla for image-guided applications in neurosurgery. *Acad Radiol* 2011;18(7):910–916.
- [4] Wang D, Strugnell W, Cowin G, Doddrell DM, Slaughter R. Geometric distortion in clinical MRI systems Part I: evaluation using a 3D phantom. *Magn Reson Imaging* 2004;22(9):1211–1221.
- [5] Michiels J, Bosmans H, Pelgrims P, Vandermeulen D, Gybels J, Marchal G, Suetens P. On the problem of geometric distortion in magnetic resonance images for stereotactic neurosurgery. *Magn Reson Imaging* 1994;12:749–765.
- [6] Stanescu T, Jans HS, Wachowicz K, Fallone BG. Investigation of a 3D system distortion correction method for MR images. *J Appl Clin Med Phys* 2010;11(1):2961.
- [7] Tanner SF, Finnigan DJ, Khoo VS, Mayles P, Dearnaley DP, Leach MO. Radiotherapy planning of the pelvis using distortion corrected MR images: the removal of system distortions. *Phys Med Biol* 2000;45(8):2117–2132.
- [8] Baldwin LN, Wachowicz K, Fallone BG. A two-step scheme for distortion rectification of magnetic resonance images. *Med Phys* 2009;36:3917–3926.
- [9] Baldwin LN, Wachowicz K, Thomas SD, Rivest R, Fallone BG. Characterization, prediction, and correction of geometric distortion in 3 T MR images. *Med Phys* 2007;34:388–399.
- [10] Schmitt F. Correction of geometrical distortions in MR-images. In *Proceedings of the Computer Assisted Radiology*, 1985, p. 15-23.
- [11] Doran SJ, Charles-Edwards L, Reinsberg SA, Leach MO. A complete distortion correction for MR images: I. Gradient warp correction. *Phys Med Biol* 2005;50:1343–1361.
- [12] Reinsberg SA, Doran SJ, Charles-Edwards EM, Leach MO. A complete distortion correction for MR images: II. Rectification of static-field inhomogeneities by similarity-based profile mapping. *Phys Med Biol* 2005;50:2651–2661.
- [13] Kannengiesser SA, Wang Y, Haacke EM. Geometric distortion correction in gradient-echo imaging by use of dynamic time warping. *Magn Reson Med* 1999;42:585–590.

- [14] Chang H, Fitzpatrick JM. A technique for accurate magnetic resonance imaging in the presence of field inhomogeneities. *IEEE Trans Med Imaging* 1992;11:319–329.
- [15] Langlois S, Desvignes M, Constans JM, Revenu M. MRI geometric distortion: a simple approach to correcting the effects of non-linear gradient fields. *J Magn Reson Imaging* 1999;9:821–831.
- [16] Morgan PS, Bowtell RW, McIntyre DJ, Worthington BS. Correction of spatial distortion in EPI due to inhomogeneous static magnetic fields using the reversed gradient method. *J Magn Reson Imaging* 2004;19(4):499–507.
- [17] Prado PJ, Blumich B, Schmitz U. One-dimensional imaging with a palm-size probe. *J. Magn. Reson.* 2000;144(2):200–206.
- [18] Casanova F, Blumich B. Two-dimensional imaging with a single-sided NMR probe. *J. Magn. Reson.* 2003;163(1):38–45.
- [19] Casanova F, Perlo J, Blumich B, Kremer K. Multi-echo imaging in highly inhomogeneous magnetic fields. *J. Magn. Reson.* 2004;166(1):76–81.
- [20] Epstein CL, Magland J. A novel technique for imaging with inhomogeneous fields. *J. Magn. Reson.* 2006;183(2):183–192.
- [21] Cho ZH, Kim DJ, Kim YK. Total inhomogeneity correction including chemical shifts and susceptibility by view angle tilting. *Med Phys* 1988;15(1):7–11.
- [22] Cho ZH, Wong EK. Fringe Field MRI. U.S. Patent 5023554.
- [23] Lu W, Pauly KB, Gold GE, Pauly JM, Hargreaves BA. SEMAC: Slice Encoding for Metal Artifact Correction in MRI. *Magn Reson Med* 2009;62(1):66–76.
- [24] Haacke EM and Brown RW and Thompson MR and Venkatesan R. *Magnetic Resonance Imaging: Physical Principles and Sequence Design*. Wiley-Liss; 1999.
- [25] Eccles CD, Crozier S, Westphal M, Doddrell DM. Temporal Spherical-Harmonic Expansion and Compensation of Eddy-Current Fields Produced by Gradient Pulses. *J Magn Reson A* 1993;103:135–141.
- [26] Janke A, Zhao H, Cowin GJ, Galloway GJ, Doddrell DM. Use of spherical harmonic deconvolution methods to compensate for nonlinear gradient effects on MRI images. *Magn Reson Med* 2004;52(1):115–122.
- [27] Sumanaweera TS, Adler JR, Napel S, Glover GH. Characterization of spatial distortion in magnetic resonance imaging and its implications for stereotactic surgery. *Neurosurgery* 1994;35(4):696–703.

- [28] Novotny J, Vymazal J, Novotny J, Tlachacova D, Schmitt M, Chuda P, Urgosik D, Liscak R. Does new magnetic resonance imaging technology provide better geometrical accuracy during stereotactic imaging? *J. Neurosurg.* 2005;102 Suppl:8–13.
- [29] Dean D, Duerk JL, Kamath JK. Geometric Distortion Correction in Magnetic Resonance Imaging. U.S. Patent 6445182 B1.

Chapter 3

A New Method: MR-based Field-of-View Extension in MR/PET

An adapted version of this chapter has been submitted:

Blumhagen JO, Ladebeck R, Fenchel M, Scheffler K. MR-based field-of-view Extension in MR/PET: B_0 Homogenization Using Gradient Enhancement. *Magnetic Resonance in Medicine 2012, in print.*

3.1 Introduction

The MR FoV is well-known to be limited in all geometric directions due to B_0 inhomogeneities and nonlinearities in the gradient field [1–7]. The limitation of the restricted MR FoV is often encountered with the patient’s arms, which can be positioned outside the nominal MR FoV. In the previous chapter the distortions were analyzed outside this usual specified FoV. In this region, strong MR signal distortions occurred. These FoV restrictions can cause a truncation of the MR image and, therefore, can bias the PET data reconstruction [8]. However, the spatial integrity of the attenuation map for attenuation and scatter correction is essential for three reasons. First, the attenuation correction factors $ACF = exp(-\int \mu(r)dr)$ for the PET emission data are computed as the line of integrals of 511keV photon attenuation μ along each line of response of the PET detector [9]. This means that slight distortion of the attenuation map of μ values can have a big impact on the ACF because of the exponential in the mentioned formula. Second, a distortion-free attenuation map is required for scatter computation [10–13]. Third, for the computation of scatter scaling a precise contour of the object needs to be known in order to identify the data region that can be used for scaling [14, 15].

Medical experts have stated that a maximum bias of 10 % with respect to PET/CT is acceptable for MR-based attenuation correction [8]. The distortion due to a PET signal attenuation of 10 % along a single line of response of a coincidence event is calculated as follows:

$$\frac{I}{I_0} = exp(-\mu(r)\Delta r) \stackrel{!}{=} 0.9 \Rightarrow \Delta r = -ln(0.9)/(0.1cm^{-1}) = 1.05cm. \quad (3.1)$$

This calculation yields an MR pixel distortion of $\Delta r = 1.05$ cm in the attenuation map, e.g. if the patient’s arm is squeezed by 1cm in the MR image, where I_0 is the initial intensity, I is the intensity after attenuation, and $\mu(r) = 0.1$ cm⁻¹ is the attenuation coefficient for soft-tissue. For a more detailed analysis additional factors must be taken into account. The magnitude by which any voxel in the reconstructed volume is affected by an error in the attenuation map is proportional to the ratio of lines of response passing through both the voxel and the erroneous area in the attenuation map. As an approximation for the given experiment, this effect can be considered to be proportional to the solid angle covered by the distorted objects outside the FoV with respect to a central voxel. As second order effects, scatter effects and potential missegmentations of fat and soft-tissue can be considered but their effect is considered to be less prominent. However, the value of Δr above can be used as an estimation of the impact of distortions on the MR-based attenuation correction. In this work, Δr is considered to be the maximum acceptable spatial error for an adequate attenuation correction.

The present work proposes a new method that compensates field imperfections

and extends the MR-based FoV. Based on measurements of both the main magnetic field and the gradient field, we were able to compute a pixel-wise prediction of distortion due to B_0 inhomogeneities and gradient nonlinearities. Analyses of these two error fields outside the specified FoV have shown the feasibility of superimposing both sources of distortion in a compensatory way. The gradient error field scales linearly with the gradient amplitude, whereas the B_0 inhomogeneity is independent of the gradient amplitude [2]. Consequently, an optimized amplitude of the readout gradient can be determined and used as a scaling parameter to reduce the distortion at a specific position [16]. This method offers an extended FoV in the transaxial plane out to 600 mm diameter on the MR part of an MR/PET system and, therefore, has the potential to extend the range of the MR-based PET attenuation correction.

3.2 Theory

The dependency of the pixel distortion on the B_0 inhomogeneity and the gradient nonlinearities in 2D spin-echo was derived in section 2.2 and validated in section 2.4. Based on these equations, an optimal gradient can be found pixel-wise to compensate the distortion due to the B_0 inhomogeneities and the distortion due to the gradient nonlinearities.

The distortion in the readout direction is

$$x' = x + \frac{\Delta B_{G_x}(x, y, z)}{G_x} + \frac{\Delta B_0(x, y, z)}{G_x} \quad (3.2)$$

where x is the actual position and x' the distorted position.

The gradient nonlinearities $\Delta \vec{G}$ scale with the gradient strength \vec{G} . Thus, the second term in Eq. 3.2 is constant and can be written as the relative gradient error:

$$\vec{c} = \frac{\Delta \vec{B}_{\vec{G}}}{\vec{G}}. \quad (3.3)$$

Therefore, the distortion in readout direction depends directly on the applied readout gradient

$$\vec{D}_{RO}(\vec{G}_{RO}) = \vec{c} + \frac{\Delta \vec{B}_0}{\vec{G}_{RO}}. \quad (3.4)$$

An optimal readout gradient can be determined to achieve zero-distortion $\vec{D}_{RO}(\vec{G}_{RO,opt}) \stackrel{!}{=} 0$ at a certain position

$$\vec{G}_{RO,opt} = -\frac{\Delta \vec{B}_0}{\vec{c}}. \quad (3.5)$$

In this chapter it is shown that this optimal readout gradient is in the range of technically feasible gradient strengths and can cause a significant distortion reduction.

3.3 Materials and Methods

3.3.1 Simulations

Simulations were performed using Matlab R2010b (The MathWorks, Inc., Natick, MA, USA). The magnetic field values were calculated using spherical harmonic expansion from the measured spherical harmonic coefficients as described in Chapter 2. Our algorithm uses the field parameters A_{nm} and B_{nm} (Eq. 2.8) as an input for further calculations. The field plot measurement has to be performed only once for a specific scanner and is, therefore, not time relevant in patient measurements. Based on the measured field values, the distortion due to the B_0 inhomogeneities and the nonlinearities of the gradient field was calculated voxel-wise for optimized and non-optimized gradients according to Eq. 3.4.

The distortion in readout direction was simulated along a line at ($x = [-0.3 \text{ m}, +0.3 \text{ m}]$, $y = 0 \text{ m}$, $z = 0 \text{ m}$) using maximum gradient strengths ($G_x = \pm 45 \text{ mT/m}$) and optimal gradient strengths ($G_{x,opt}(x = -0.3 \text{ m}) = -5.38 \text{ mT/m}$ and $G_{x,opt}(x = +0.3 \text{ m}) = 2.84 \text{ mT/m}$) for distortion reduction at the left and the right edge of the extended FoV. No post-processing distortion correction was applied. A distortion simulation in the slice-select direction along the same line was performed for gradient amplitudes of $G_z = \pm 45 \text{ mT/m}$, $G_{z,opt}(x = -0.3 \text{ m}) = -43.0 \text{ mT/m}$, and $G_{z,opt}(x = +0.3 \text{ m}) = -15.34 \text{ mT/m}$. Furthermore, the distortion in the readout direction was calculated along a line at ($x = 0.28 \text{ m}$, $y = 0 \text{ m}$, $z = [-0.12 \text{ m}, +0.12 \text{ m}]$) using gradient amplitudes of $G_x = \pm 45 \text{ mT/m}$ and $G_{x,opt}(z = 0 \text{ m}) = 2.86 \text{ mT/m}$. The distortion in the slice-select direction along the same line was simulated using gradient amplitudes of $G_z = \pm 45 \text{ mT/m}$, $G_{z,opt}(z = -0.09 \text{ m}) = 3.36 \text{ mT/m}$, and $G_{z,opt}(z = +0.09 \text{ m}) = -5.42 \text{ mT/m}$.

The optimal readout gradient strength and the optimal slice-select gradient strength causing zero-distortion were calculated according to Eq. 3.5 one-dimensionally along a line at ($x = 0.28 \text{ m}$, $y = 0 \text{ m}$, $z = [-0.12 \text{ m}, +0.12 \text{ m}]$). Furthermore, the optimal readout gradient was determined voxel-wise in three dimensions (x , $y = [-0.3 \text{ m}, 0.3 \text{ m}]$, $z = [-0.15 \text{ m}, +0.15 \text{ m}]$) and plotted for cylinder volumes at typical patient's arm positions at ($x = \pm 0.26 \text{ m}$, radius = 0.04 m , length = 0.3 m).

The slice profiles of 7 slices ($z = [-0.12 \text{ m}, +0.12 \text{ m}]$, distance of 40 mm , thickness of 5 mm) were simulated in an extremely extended FoV (0.646 m diagonal) using the maximum slice-select gradient of $G_z = 45 \text{ mT/m}$ and a gradient strength $G_{z,opt}(z = -0.04 \text{ m}) = 5 \text{ mT/m}$ optimized for slice position $z = -0.04 \text{ m}$.

3.3.2 Sequence Design

A modified multislice 2D spin-echo-based sequence was developed featuring the calculation and the automatic use of the optimal readout gradient amplitude for each slice individually [17]. The field parameters were read from an input coefficients file based on the measurements described above. The B_0 inhomogeneities and the readout gradient nonlinearities were calculated for each optimization region and each slice position using spherical harmonic field expansion (Eq. 2.8). The optimal readout gradient amplitudes were calculated according to Eq. 3.5 and adjusted automatically. No further user interactions were needed.

A detailed description of the sequence design, called HUGE (B_0 Homogenization Using Gradient Enhancement), is given in chapter 4.

3.3.3 Phantom Studies

HUGE achieves a distortion reduction at a region of interest which is preferably as large as the patient's arm. The feasibility of achieving a sufficient image fidelity was confirmed using an arm-like tube phantom. The structure of the patient's arm was assumed to be homogeneous in the z-direction. Therefore,



Figure 3.1: Structure phantom consisting of 43 tubes of 13 mm in diameter each. The tube phantom, 130 mm in diameter and 650 mm in length, was built to model a patient's arm.

such a structure phantom (diameter: 130 mm, length: 650 mm, homogeneous in z-direction, filled with $1.25 \text{ g NiSO}_4 \times 6\text{H}_2\text{O} + 5 \text{ g NaCl}$ per 1000 g H_2O)

was built with 43 tubes, each with 13 mm in diameter, to model a patient's arm (Fig. 3.1). The phantom was placed outside the normal specified FoV at ($x = \pm 0.3$ m). Transversal planes were acquired with an in-plane resolution of $1.56 \times 1.56 \text{ mm}^2$, slice thickness $SL = 5$ mm, echo time $TE = 7.7$ ms, repetition time $TR = 300$ ms. A quantification of image fidelity determined as percentage deviation from reference measurement at iso-center position was performed for optimized and non-optimized gradient amplitudes.

3.3.4 *In Vivo* Studies

In vivo experiments were performed on healthy volunteers. MR measurements were acquired on a 3T Biograph mMR system (Siemens Healthcare, Erlangen, Germany). The scanner and coil hardware were not adapted. Maximum amplitude achievable by the gradient system was 45 mT/m and the maximum slew rate was 200 T/m/s. The volunteer's arms were placed as far apart as possible ($x = \pm 0.3$ m). At the outer positions, the patient's arms could not be covered completely by a local coil. To demonstrate the feasibility of the proposed method in clinical routine, only the body coil was used as transmit/receive coil and a corresponding loss in signal to noise ratio was accepted. The FoV was set to 600mm with $1.88 \times 1.88 \text{ mm}^2$ in-plane resolution and 5 mm slice thickness. Informed consent was obtained from all volunteers.

3.4 Results

3.4.1 Distortion in an extended FoV

Using non-optimized gradients, strong distortions were observed at off-center positions in an extended FoV of up to 600 mm in diameter. Figure 3.2 shows typical pixel-distortions of the tube phantom placed at the off-center position $x = -0.3$ m. Small distortions at the edges of the specified FoV were usually removed by a regular post-processing distortion correction, which was not applied in this experiment. However, in the extended FoV the distorted pixels were squeezed so strongly that correcting them by a post-processing method was not possible at the spatial resolution of clinical MR images. In the coronal view the structure inside the phantom was vertical. The strength and the polarity of the observed distortion, which was identified as a deviation from the ideal vertical lines, was position-dependent. Swapping the readout gradient polarity changed the polarity of the distortion direction in readout direction.

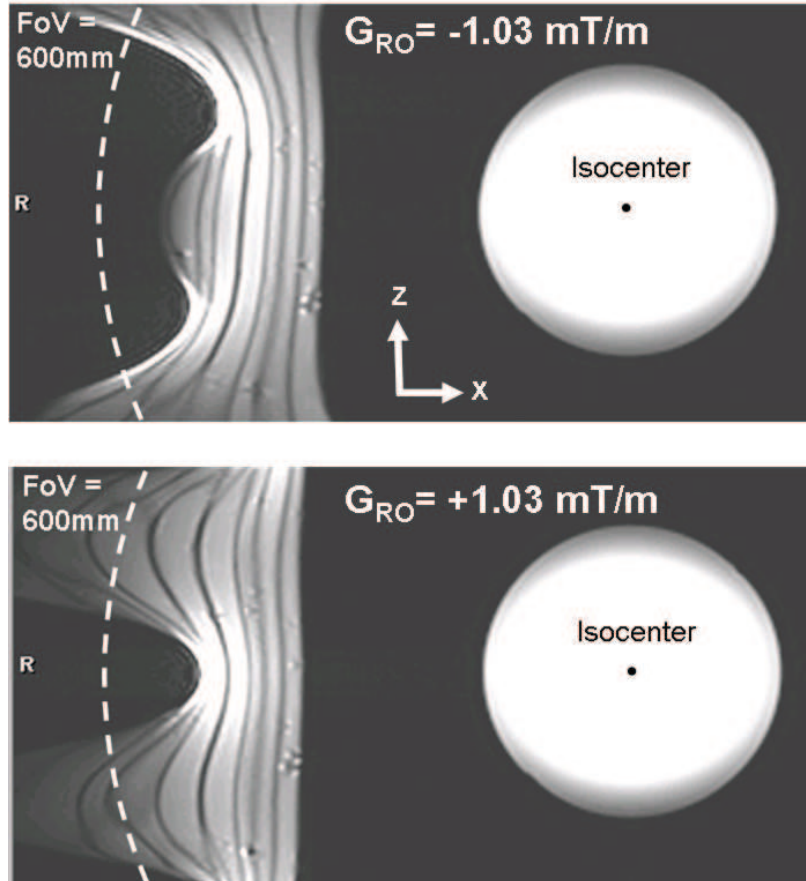


Figure 3.2: Off-center measurement, coronal plane. The spherical phantom was placed at iso-center position and the tube phantom was aligned to the z-axis touching the body coil at position $x = -300$ mm outside the specified FoV. No post-processing distortion correction was applied. Readout gradients were $G_x = 1.03$ mT/m (above) and $G_x = -1.03$ mT/m (below). In readout direction, the polarity swap of the readout gradient flipped the distortion direction.

3.4.2 Field Measurements and Simulations

All simulations were based on measured field values. The field plots are shown in Fig. 3.3. The observed pattern of the inhomogeneity of the main magnetic field ΔB_0 (Fig. 3.3A) and the pattern of the nonlinearity of the x-gradient field ΔG_x (Fig. 3.3B) are similar both with respect to symmetry in z-direction ($\Delta B_0(x, y, +z) = \Delta B_0(x, y, -z)$ and $\Delta G_x(x, y, +z) = \Delta G_x(x, y, -z)$) and with respect to the position of roots ($\Delta B_0(x = \pm 0.3m, y = 0m, z \approx \pm 0.04m) = 0$ and $\Delta G_x(x = \pm 0.3m, y = 0m, z \approx \pm 0.04) = 0$), whereas the pattern of the nonlinearity of the z-gradient field (Fig. 3.3C) is different both with respect to symmetry ($\Delta G_z(x, y, +z) = -\Delta G_z(x, y, -z)$) and to position of roots ($\Delta G_z(x = \pm 0.3m, y = 0m, z \approx (-0.06m, 0m, 0.06m)) = 0$).

The distortion in the readout direction (Fig. 3.4A) depends strongly on the readout gradient strength at the edges of the extended FoV ($|x| > 0.25$ m), whereas no significant influence of the gradient was observed on the distortion at iso-center position. Using the optimal readout gradient amplitude results in a significant distortion reduction of up to 0.03m and a maximum residual distortion of 0.01m compared to using the maximum readout gradient. The distortion in the slice-select direction (Fig. 3.4B) was reduced by 4mm to a maximum residual distortion of below 2 mm for $x > +0.25$ m using the optimal slice-select gradient. In the region of $x < -0.25$ m the distortion was already below 1 mm using the maximum gradient strength and thus was not further reduced significantly.

The z-dependency of the distortion in the readout direction at ($x = 0.28$ m, $y = 0$ m, $z = [-0.12$ m, 0.12 m]) is shown in Fig. 3.4C. Using the readout gradient optimized for the $z = 0$ m position reduced the distortion at this position as specified but also reduced the distortion at a region of $z = [-0.1$ m 0.1 m] compared to the maximum readout gradient strength. Figure 3.4D shows the distortion in the slice-select direction as a function of z-position at the same off-center position. The maximum gradient strength caused no distortion at the $z=0$ m position, whereas for other z-positions a significant distortion reduction (0.028 m at $z = -0.09$ m and 0.014 m at $z = +0.09$ m) was achieved by optimized gradients.

The optimal gradient strengths corresponding to zero-distortion at ($x = 0.28$ m, $y = 0$ m, $z = [-0.12$ m, 0.12 m]) were observed to be in the range of ± 8 mT/m for the readout gradient (Fig. 3.4E) and ± 20 mT/m for the slice-select direction (Fig. 3.4F) with few exceptions. The exceptions were poles in the function of optimal gradients. Here, the nonlinearity tended faster toward zero than the B_0 inhomogeneity at the z-positions of $z \approx \pm 0.03$ m for the readout gradient and $z \approx 0$ m for the slice-select gradient and thus the optimal readout gradient increased according to (Eq. 3.5). However, the distortion in readout direction (Fig. 3.4C) was acceptably low and independent of the gradient strength at these positions ($z \approx \pm 0.03$ m) due to low amount of nonlinearity and B_0 inho-

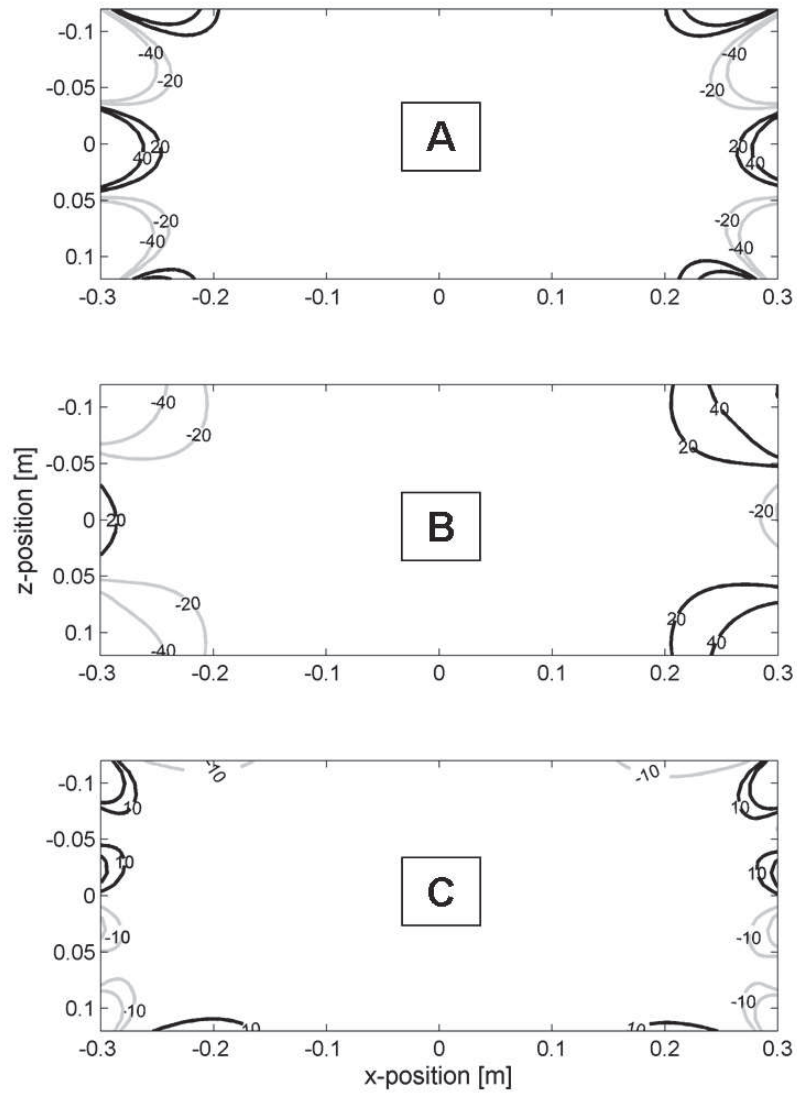


Figure 3.3: Contour plots of measured field values. B_0 inhomogeneity of the main magnetic field (A), nonlinearity of the x-gradient ΔB_{G_x} (B) and of the z-gradient ΔB_{G_z} (C) are shown (isolines in μT). Coronal view of an extremely extended FoV (0.646m diagonal).

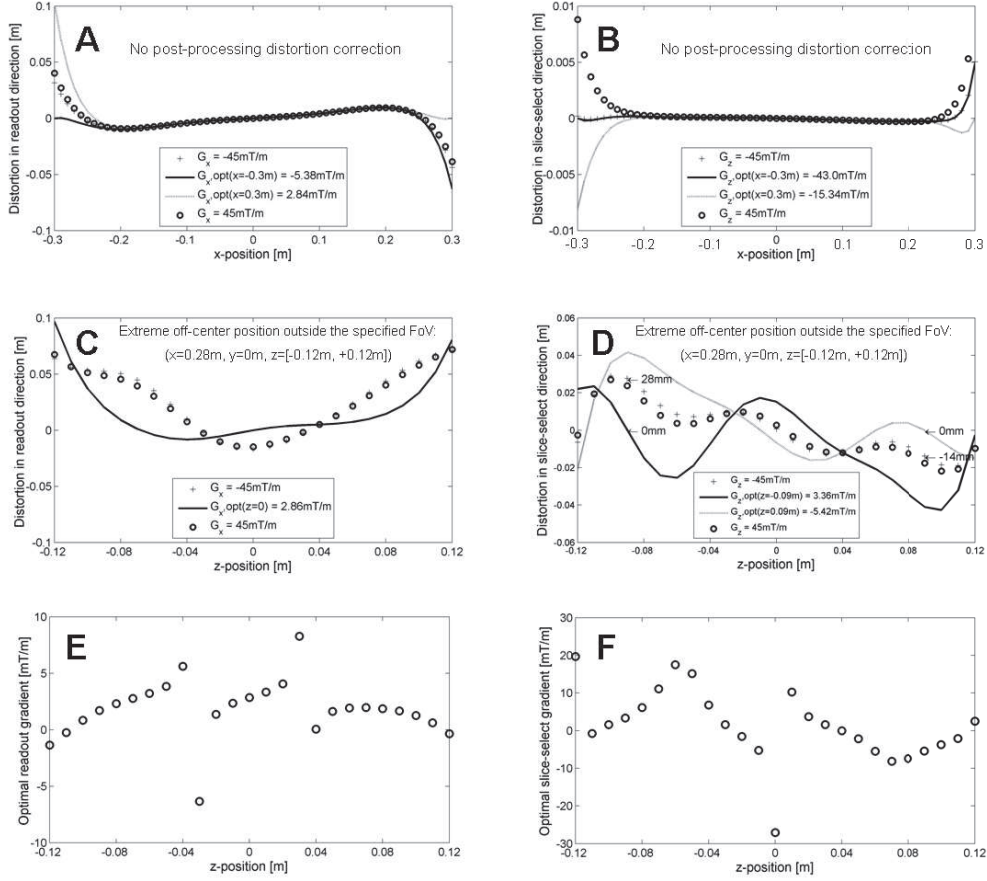


Figure 3.4: Distortion in readout direction (A) and slice-select direction (B) were simulated along a line at ($x = [-0.3\text{ m } +0.3\text{ m}]$, $y = 0\text{ m}$, $z = 0\text{ m}$) for the maximum gradient amplitudes of $\pm 45\text{ mT/m}$ and for the gradient amplitudes optimized for off-center positions at $z = \pm 0.3\text{ m}$. There was no post-processing distortion correction applied. Simulation of distortion are shown for readout direction (C) and slice-select direction (D) as a function of z-position at extreme off-center positions ($x = 0.28\text{ m}$, $y = 0\text{ m}$, $z = [-0.12\text{ m}, +0.12\text{ m}]$) using the maximum gradient amplitudes and the gradient amplitudes optimized for slice position $z = 0\text{ m}$ and $z = \pm 0.09\text{ m}$. Optimal readout gradients (E) and optimal slice-select gradients (F) corresponding to zero-distortion were calculated as a function of z-position ($x = 0.28\text{ m}$, $y = 0\text{ m}$, $z = [-0.12\text{ m } +0.12\text{ m}]$).

mogeneity (Fig. 3.3A,B). The distortion reduction in slice-select direction (Fig. 3.4D) was improved by a strong gradient due to low amount of nonlinearity (Fig. 3.3C) and non-negligible amount of B_0 inhomogeneity (Fig. 3.3A) at this position ($z \approx 0$ m).

In the previous chapter, it was shown that the frequency mapping might fail

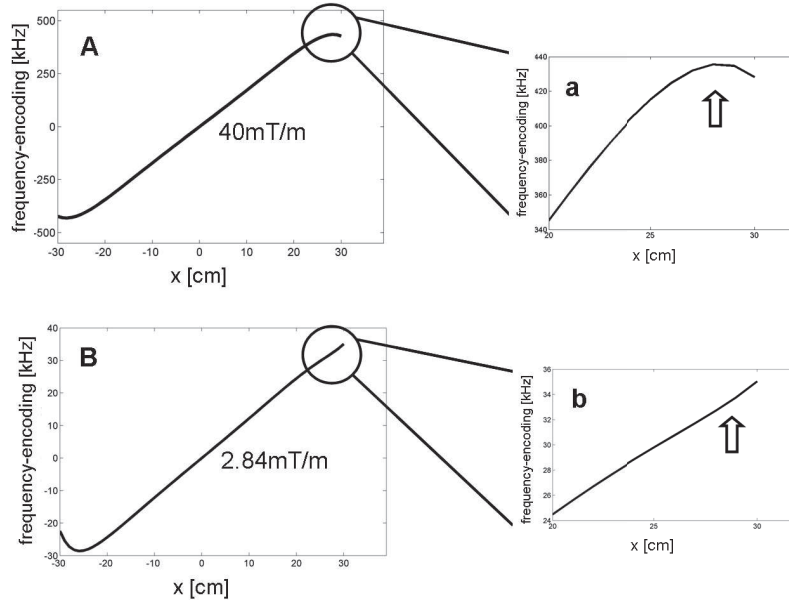


Figure 3.5: Simulation of frequency mapping based on the measured field coefficients. The x-gradient is plotted for an extended range in the x-direction ($-30 \text{ cm} < x < 30 \text{ cm}$, $y = 0 \text{ m}$, $z = 0 \text{ m}$). While the x-gradient is linear within the specified FoV (A), the slope decreases significantly and is even inverted at an extreme off-center position (a) using the maximum gradient amplitude of 40 mT/m . A linear slope was achieved even outside the specified FoV using a readout gradient amplitude of 2.84 mT/m (B) optimized for this specific region of interest at off-center position (b).

at off-center positions outside the usual specified FoV (Fig. 3.5A,a). The simulated frequency-encoding is shown one-dimensionally for the x-axis ($-30 \text{ cm} < x < 30 \text{ cm}$, $y = 0 \text{ m}$, $z = 0 \text{ m}$). Using a strong readout gradient of $G_x = 40 \text{ mT/m}$ the achieved frequency dependency became nonlinear at very off-center positions ($x > 25 \text{ cm}$). The slope of the gradient decreased significantly with increasing distance from iso-center and was even inverted at position $x = 29 \text{ cm}$. Using a readout gradient amplitude optimized for a specific region of interest a linear slope was achieved even outside the specified FoV (Fig. 3.5B,b). Furthermore, the voxel-wise simulation of the optimal readout gradient showed that the values within the volume of cylinders, which modeled the patient's arms with respect to the dimensions and the positions, were in the range of technically feasible

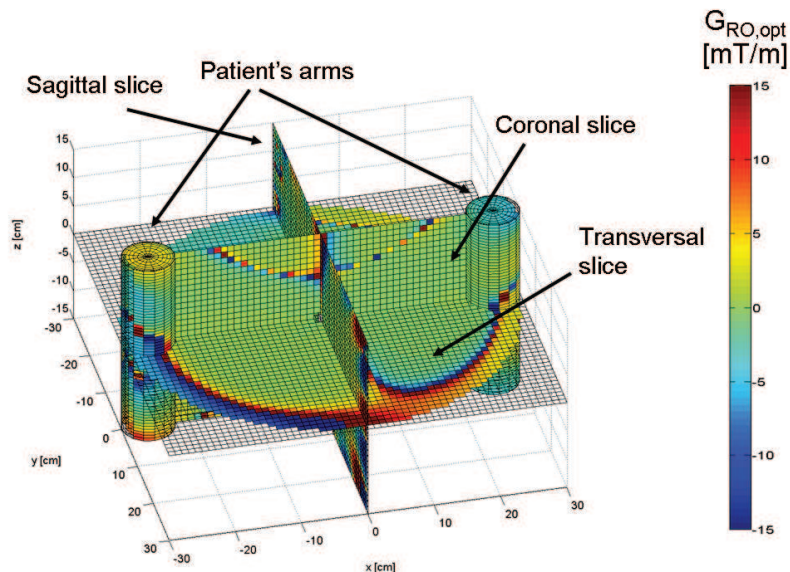


Figure 3.6: Voxel-wise simulation of the optimal readout gradients $G_{RO,opt}$ [mT/m]. Main Cartesian planes ($x, y = \pm 300$ mm, $z = \pm 150$ mm) and arm-like tubes (radius = 40 mm, length = 300 mm) are plotted. Voxel resolution is 1 cm^3 .

gradient strengths for clinical scanners (Fig. 3.6).

The simulation of slice profiles showed distortions in slice-select direction and changes in slice thickness at the edges of an extended FoV (Fig 3.7). The distortion of the slice at $z = -0.04$ m excited by the maximum gradient strength (Fig. 3.7A) was significantly reduced by the optimal gradient amplitude (Fig 3.7B), whereas the slice thickness tended to decrease with respect to distance from iso-center.

3.4.3 Phantom Experiments

A quantification of the readout gradient dependency on the distortion in readout direction was achieved in simulations and in phantom experiments. The optimal readout gradient caused a change of the space-dependent distortion. Figure 3.8 shows the pixel-wise distortions for a transversal plane at $z = 0$ m using optimized and non-optimized gradients for the usual position of the right patient's arm ($x = -0.3$ m, $y = 0$ m). The distortion is locally reduced to zero at a specific position but may be higher at other positions. In the phantom study, we observed a significant overall distortion reduction in a region of interest dimensioned as large as a patient's arm. Using a non-optimized readout gradient

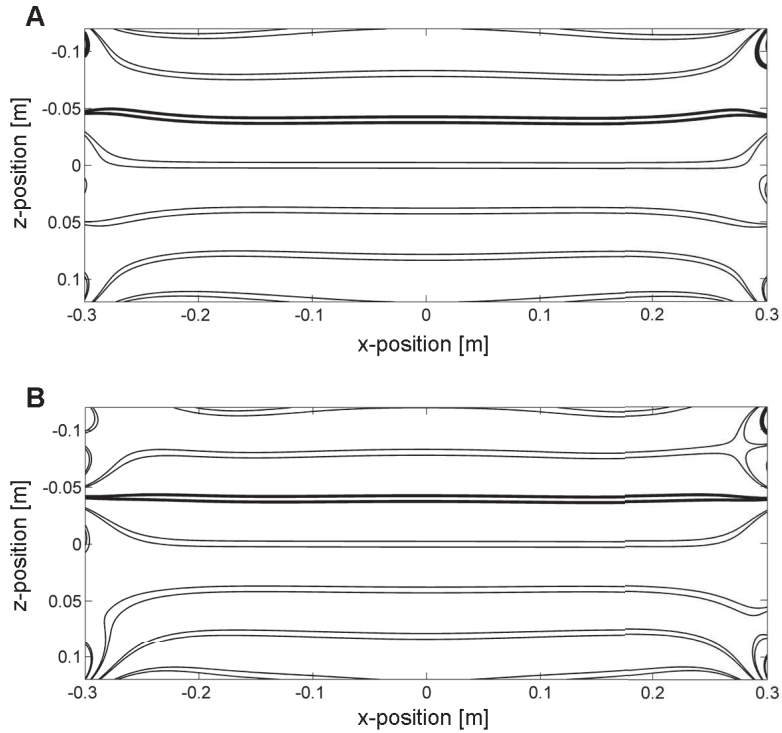


Figure 3.7: Simulation of slice profiles using a slice-select gradient of $G_z = +45$ mT/m (A) and $G_z = 5$ mT/m (B). Excitation frequencies and bandwidth were set to simulate slice profiles of 2mm thickness at positions $z = (-0.12$ m, -0.08 m, -0.04 m, 0 m, $+0.04$ m, $+0.08$ m, $+0.12$ m) in an extremely extended FoV (0.646 m diagonal). The gradient amplitude in (B) was determined to reduce the distortion of the highlighted slice profile at position $z = -0.04$ m.

in amplitude and polarity of $G_x = 2.48$ mT/m caused a distortion-related deviation of 32.1 % from the reference measurement at iso-center position (Fig. 3.8a). A non-optimized gradient amplitude of $G_x = -5$ mT/m resulted in a deviation of 15.4 % (Fig. 3.8b). HUGE decreased the overall deviation to 8.5 % by applying one single optimized readout gradient, here $G_{x,opt} = -2.48$ mT/m, for the entire region of interest (Fig. 3.8c).

3.4.4 Volunteer Experiments

Distortion reduction of both patient arms was achieved. Figure 3.9 shows a transversal plane of the patient's arms. In the non-optimized mode, the patient's arms were significantly distorted outside the normal specified FoV. Several pixels were squeezed. Using HUGE, adapting the optimal readout gradients for imaging at off-center positions allowed for a distortion-reduced acquisition

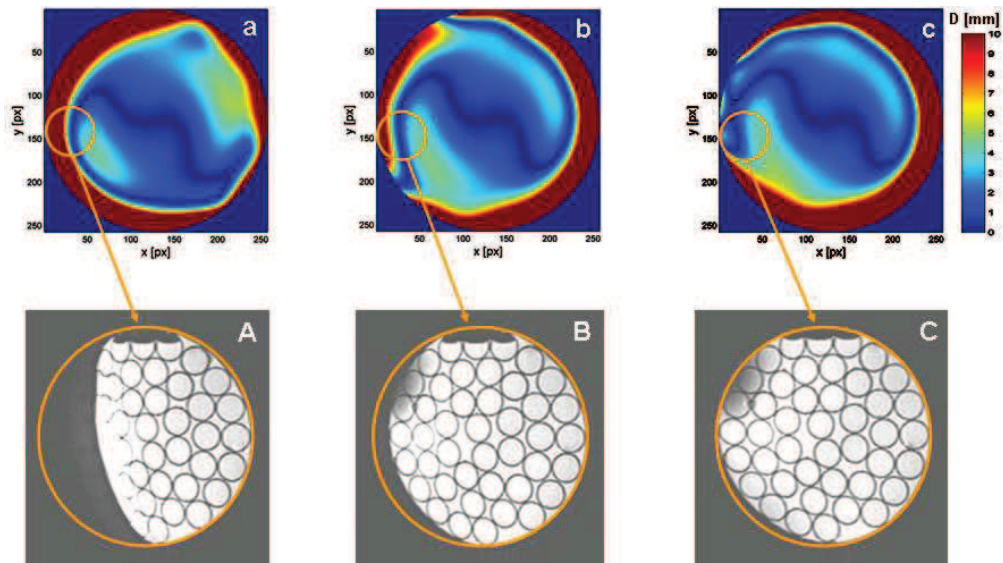


Figure 3.8: Pixel-wise simulation of distortions D [mm] in readout direction for an extremely extended FoV (a-c) and corresponding measurements of the tube phantom touching the body coil at position $x = -300$ mm (A-C). Transversal plane at $z = 0$ m, matrix size is 256^2 . Readout gradient strengths are $G_x = +2.48$ mT/m (A), $G_x = -5$ mT/m (B) and $G_x = -2.48$ mT/m (C). There was no additional post-processing distortion correction applied.

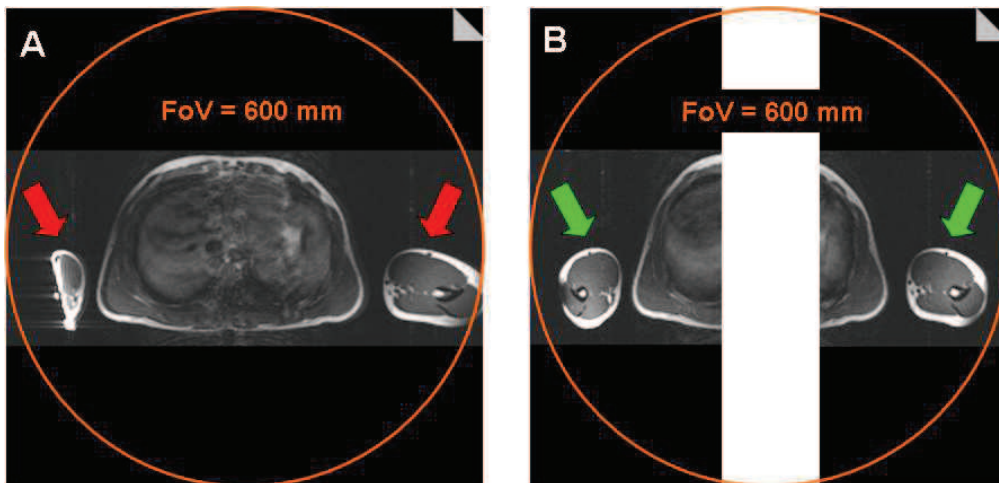


Figure 3.9: Transversal slice, field-of-view: 600mm. Typical distortions of the patient's arms located at off-center positions (A) were reduced using an optimal readout gradient for the left and right patient's arm (B).

of both arms of the patient.

3.5 Discussion

The proposed sequence-based imaging technique, HUGE, offers a significant in-plane distortion reduction in the presence of gradient nonlinearities and B_0 inhomogeneities. Distortions at off-center positions can be reduced using an optimal space-dependent readout gradient. Even outside the normal specified FoV, a significant distortion reduction was achieved in simulations, in phantom and in volunteer measurements.

The conventional procedure in distortion reduction is the use of very large gradients. This simple approach reduces the B_0 influence but not the distortion caused by the nonlinearity of the gradient field. However, the distortion is tolerably small within the normal FoV and can be further corrected in post-processing. This is not the case at the edges of an extended FoV. Here, the distortions are very large and several pixels might superimpose so that a robust post-processing distortion correction cannot be achieved. The imaging technique presented in this work reduced the source of distortion before spatial encoding. An optimal readout gradient can be determined such that the distortion caused by the B_0 inhomogeneities compensates the distortion caused by the gradient nonlinearities. Furthermore, the optimal gradient strength was typically much smaller than the maximum gradient strength and thus allowed for a higher signal-to-noise ratio.

The dependency of the in-plane distortion in the frequency-encoding direction on the applied readout gradient amplitude, as described by Bakker et al. [2], was confirmed in the phantom experiment. The observed distortion in the phantom experiment was consistent with the results obtained in simulations. These simulations were performed based solely on measurements of the gradient field and the B_0 field. Thus, the measured distortion in the phantom experiments can be fully explained by the nonlinearities of the gradient field and the B_0 inhomogeneities. Consequently, the measured values for the magnetic fields and the aforementioned dependency of the readout gradient on the distortion is sufficient to determine the optimal readout gradient amplitude.

Although the overall spatial variation of the B_0 field is of much higher order than that of the gradient fields, the variation of the readout gradient (x-gradient) is comparable to that of the main magnetic field regarding symmetry and position of roots at the region of interest $z = [-0.12 \text{ m}, +0.12 \text{ m}]$, which covers the range of a typical PET FoV in z-direction. Consequently, the distortion in readout direction can be reduced at a region, which is acceptably large in terms of cross-section of the patient's arm and slice thickness, by using only one single optimal readout gradient. In simulations, the readout gradient optimized for the $z = 0 \text{ m}$ position reduced the distortion significantly along a line at $z = \pm 0.08 \text{ m}$

and in-plane for a cross-section of a patient's arm. The phantom and volunteer experiments confirmed that significant distortion reductions can already be achieved outside the specified FoV by applying only one single readout gradient per arm position and per slice. Furthermore, the voxel-wise simulation showed that the optimal readout gradients are in the range of technically feasible gradient strengths.

The spatial variation pattern of the slice-select gradient (z-gradient) is different in symmetry and does not adequately match that of the main magnetic field. Although an optimal slice-select gradient was found for each z-position and the distortion was reduced in simulations, a residual change in slice thickness was observed at the edges of simulated slice profiles. However, in a first approximation the structure of the patient's arm can be assumed to be homogeneous in the z-direction. Thus, for the purpose of this study, which is the improvement of the MR-based attenuation correction, an adequate in-plane distortion reduction in the extended FoV is sufficient. The requirement of a distortion below 1cm, as defined in the introduction of this chapter, was fulfilled. Furthermore, the required resolution for an accurate MR-based attenuation correction given by the PET resolution, which is limited to about 2 mm^2 by the PET crystal geometry, was achieved in phantom and volunteer experiments. Again, the presented technique provides MR data of regions outside the normal FoV for an improved MR-based attenuation correction of PET data. It does not provide MR images for clinical diagnosis. If such an image quality is required, the distortion in slice-select direction has to be taken into account and a distortion reduction by an optimized slice-select gradient and RF pulse has to be considered.

Due to the system-dependent architecture of the main magnetic field coil and the gradient coil and an individual iron configuration of the passive shim, the pattern of field imperfections outside the specified FoV differs from system to system. Thus, a system-specific coefficient file of gradient nonlinearities and B_0 inhomogeneities was obtained from individual measurements for each system and was provided to the user.

The sequence implementation is based on a multi-slice spin echo sequence and allows for an individual optimal readout gradient amplitude for each slice. The acquisition time was 43 s per arm position for each bed position and was thus short enough to allow the proposed method in clinical routine.

The proposed technique can reduce the distortion in the readout direction, but not in the phase-encoding direction. As Eq. 2.6 shows, the B_0 inhomogeneities do not cause a distortion in the phase-encoding direction and can therefore not be used to compensate gradient-related distortions. For the purpose of imaging the patient's arms outside the specified FoV at typical positions ($x = \pm 0.3 \text{ m}$, $y \approx 0 \text{ m}$), it is essential to assign the phase-encoding direction to the y-direction. The patient's arms are nearly at the center-position related to the y-direction. Nonlinearities of the y-gradient coil at this position can thus be neglected.

In MR/PET, the additional image data in an extended MR-based FoV acquired

with HUGE can be used to support the PET attenuation correction. It involves four steps. First, a single measurement of the system-specific gradient nonlinearities and B_0 inhomogeneities. Second, the calculation of the space-dependent optimal readout gradient amplitude. Third, the scan of multiple transversal slices using the individual optimal gradient amplitudes. Fourth, processing the additional information, that is the position and undistorted structure of patient's arm, for the PET attenuation correction.

HUGE has the potential to decrease the reported bias of the PET data reconstruction [8]. Hence, it is of interest for any kind of whole-body MR/PET examinations, performed either simultaneously in one integrated system or sequentially in two separate systems. In addition, an extended FoV could also be relevant for radiotherapy and biopsy.

3.6 Conclusion

In conclusion, a function was implemented in the multi-slice spin-echo-based sequence which calculates and adapts the optimal readout gradient for each slice and arm position. No hardware modifications were required and no further user interactions were needed. Distortion-reduced acquisitions of the patient's arms at typical off-center positions have been achieved. Therefore, HUGE has the potential to improve MR-based PET attenuation correction.

In the following chapter, HUGE is further improved concerning measurement time and FoV extension in z-direction. The use of a bipolar dual-echo implementation allows to scan both arm positions simultaneously by applying both individual optimal readout gradient amplitudes during one excitation interval thereby saving additional acquisition time [18]. A combination of the presented method and a continuously moving-table technique [19] extends the FoV in transaxial and longitudinal direction and is presented in the following chapter. Finally, in chapter 5 the developed technique is used in whole-body MR/PET examinations of patients to validate the improvement on the PET reconstruction.

References

- [1] Schmitt F. Correction of geometrical distortions in MR-images. In Proceedings of the Computer Assisted Radiology, 1985, p. 15-23.
- [2] Bakker CJ, Moerland MA, Bhagwandien R, Beersma R. Analysis of machine-dependent and object-induced geometric distortion in 2DFT MR imaging. *Magn Reson Imaging* 1992;10:597-608.

- [3] Wald L, Schmitt F, Dale A. Systematic Spatial Distortion in MRI due to Gradient Non-Linearities. *NeuroImage* 2001;13(6):50.
- [4] Dammann P, Kraff O, Wrede KH, Ozkan N, Orzada S, Mueller OM, Sandalcioglu IE, Sure U, Gizewski ER, Ladd ME, Gasser T. Evaluation of hardware-related geometrical distortion in structural MRI at 7 Tesla for image-guided applications in neurosurgery. *Acad Radiol* 2011;18(7):910–916.
- [5] Wang D, Strugnell W, Cowin G, Doddrell DM, Slaughter R. Geometric distortion in clinical MRI systems Part I: evaluation using a 3D phantom. *Magn Reson Imaging* 2004;22(9):1211–1221.
- [6] Michiels J, Bosmans H, Pelgrims P, Vandermeulen D, Gybels J, Marchal G, Suetens P. On the problem of geometric distortion in magnetic resonance images for stereotactic neurosurgery. *Magn Reson Imaging* 1994;12:749–765.
- [7] Stanescu T, Jans HS, Wachowicz K, Fallone BG. Investigation of a 3D system distortion correction method for MR images. *J Appl Clin Med Phys* 2010;11(1):2961.
- [8] Delso G, Martinez-Moeller A, Bundschuh RA, Nekolla SG, Ziegler SI. The effect of limited MR field of view in MR/PET attenuation correction. *Med Phys* 2010;37:2804–2812.
- [9] Bailey DL and Townsend DW and Valk PE and Maisey MN. *Positron emission tomography: basic sciences*. Springer; 2005.
- [10] Ollinger JM. Analytic correction for scatter in fully 3D PET: statistical issues. *Nuclear Science Symposium, 1997. IEEE* 1997;2:1386–1389.
- [11] Watson CC, Newport D, Casey ME. A single scatter simulation technique for scatter correction in 3D PET. in *Three-Dimensional Image Reconstruction in Radiology and Nuclear Medicine* (P. Grangeat and J-L. Amans, eds.), Dordrecht: Kluwer, 1996.
- [12] Watson CC, Newport D, Casey ME, deKemp RA, Beanlands RS, Schmand M. Evaluation of simulation-based scatter correction for 3-D PET cardiac imaging. *IEEE Trans. Nuc. Sci.* 1997;44:90–97.
- [13] Watson CC. New, faster, image-based scatter correction for 3D PET. *IEEE Trans. Nucl. Sci.* 2000;47:1589–94.
- [14] Watson CC, Casey ME, Michel C, Bendriem B. Advances in scatter correction for 3D PET/CT. *Nuclear Science Symposium Conference Record, 2004 IEEE* 2004;5:3008–3012.
- [15] Thielemans K, Manjeshwar R, Jansen F, Tsoumpas C. A new algorithm

for scaling of PET scatter estimates using all coincidence events . Nuclear Science Symposium Conference Record, 2007 IEEE 2007;5:3586–3590.

- [16] Blumhagen JO, Ladebeck R, Fenchel M, Kampmeier J, Scheffler K. MR-based Field-of-View Extension: Compensation of Field Imperfections. In Proceedings of the 19th Annual Meeting of ISMRM, Montreal, Quebec, Canada, 2011. p. 2693.
- [17] Blumhagen JO, Ladebeck R, Fenchel M, Scheffler K. Multislice 2D spin echo imaging using adapted readout gradients for compensation of BO inhomogeneities and gradient nonlinearities. In Proceedings of the 28th Annual Meeting of ESMRMB, Leipzig, Germany, 2011. p. 604.
- [18] Blumhagen JO, Ladebeck R, Fenchel M, Scheffler K. MR-based axial field-of-view extension: Bipolar dual-echo spin echo imaging using automatically optimized readout gradients. In Proceedings of the 28th Annual Meeting of ESMRMB, Leipzig, Germany, 2011. p. 611.
- [19] Fautz HP, Kannengiesser SA. Sliding multislice (SMS): a new technique for minimum FOV usage in axial continuously moving-table acquisitions. *Magn Reson Med* 2006;55:363–370.

Chapter 4

Implementation

Adapted versions of the following sections have been presented:

Blumhagen JO, Ladebeck R, Fenchel M, Scheffler K. Multislice 2D spin echo imaging using adapted readout gradients for compensation of B_0 inhomogeneities and gradient nonlinearities. Proceedings of the 28th Annual Meeting of ESMRMB, Leipzig, Germany, 2011.

Blumhagen JO, Ladebeck R, Fenchel M, Scheffler K. MR-based axial field-of-view extension: Bipolar dual-echo spin echo imaging using automatically optimized readout gradients. Proceedings of the 28th Annual Meeting of ESMRMB, Leipzig, Germany, 2011.

Blumhagen JO, Ladebeck R, Fenchel M, Scheffler K, and Quick HH. MR-based FoV Extension in Whole-Body MR/PET Using Continuous Table Move. Proceedings of the 20th Annual Meeting of ISMRM, Melbourne, Australia, 2012.

4.1 Introduction

In the previous chapter, a method was proposed featuring an MR-based FoV extension using an optimized readout gradient amplitude. This optimal readout gradient amplitude allowed for a compensation of the distortion due to B_0 inhomogeneity and gradient nonlinearity. Thus, the distortion was significantly reduced at specific positions outside the usual specified FoV. Furthermore, it was shown that a total distortion reduction was achieved at a region of interest as large as the patient's arm using one single optimal gradient amplitude. However, this optimal readout gradient amplitude is space-dependent and differs both for the slice position (z-position) and the arm position (x-position). To make MR acquisitions with optimal and different readout gradient amplitudes for each slice position and arm position fast enough for clinical routine, new implementation concepts and sequence designs are required.

In this work three different implementation approaches of an MR-based FoV extension were developed. The objectives were a significant distortion reduction, a sufficient volume coverage of the patient's body parts located outside the usual specified FoV and an acquisition time short enough for clinical routine. All sequence designs were spin-echo-based to ensure a sufficient signal rephasing in face of very strong B_0 inhomogeneities.

A multislice 2D spin-echo-based sequence was developed that calculates and adapts the readout (RO) gradient for each slice position automatically and offers an extended FoV in multiple slices during one single scan. However, the optimal RO gradient depends on the position of the region of interest and therefore differs for optimization of the left and the right patient's arm. Thus, a 2D SE-based sequence was implemented using a dual-echo acquisition with optimized RO gradients for distortion-reduced imaging of both the left and the right patient's arm. Nevertheless, the optimal gradient amplitude has to be modified for each slice position. However, the number of slice positions can be reduced to one using Continuous Table Movement (CTM) [1–5]. Finally, a combination of the mentioned transaxial FoV extension and CTM is presented. In experiments on volunteers, a significant distortion reduction has been achieved at off-center positions of up to 300 mm off from the iso-center.

4.2 Materials and Methods

4.2.1 Sequence Design 1: Automatic Selection of Optimal Readout Gradient in Multi-Slice Spin-Echo

A multislice 2D spin-echo-based sequence was developed that calculates and adapts the optimal readout gradient amplitude for each slice individually [6].

The use of the spin echo condition avoids signal loss caused by dephasing in the presence of B_0 inhomogeneities. As shown in Fig. 4.1, the sequence consists

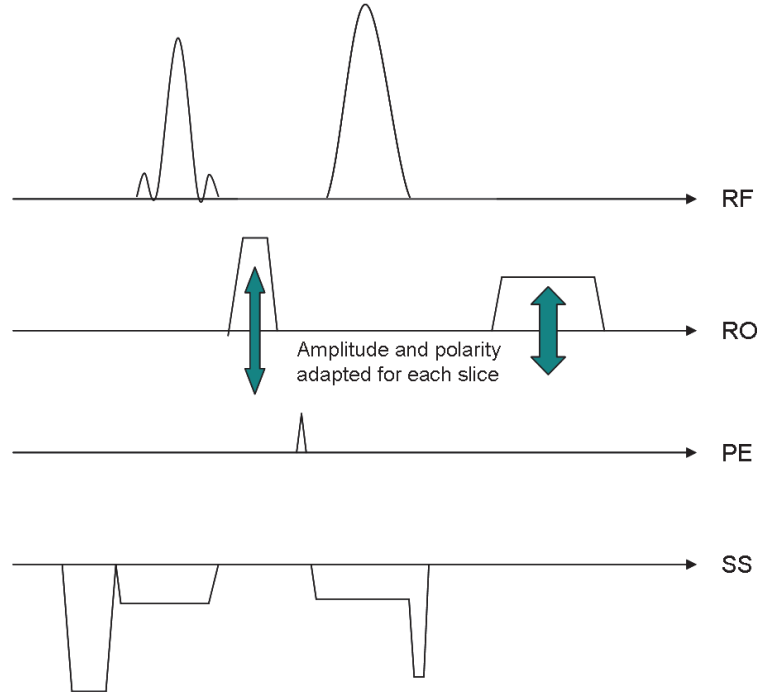


Figure 4.1: Diagram of a multislice spin-echo-based sequence. The applied radiofrequency (RF) and the gradients in readout direction (RO), phase-encoding direction (PE) and slice-select direction (SS) are shown schematically. The strength and the polarity of the optimal readout gradient are calculated and adapted for each slice and patient arm's position. The prephase gradient moment is adjusted accordingly to allow for a rephased signal at $t = TE$.

of a generic slice-select and a phase-encoding gradient. The readout gradient amplitude and the prephase moment are adapted to fulfill the following requirements:

- Accurate frequency mapping in 2D spatial encoding, despite field inhomogeneities and gradient nonlinearities. This is achieved by compensation of frequency mismapping due to B_0 phase offsets and gradient nonlinearities. The readout gradient amplitude is calculated according to (Eq. 3.5).
- Maintenance of the conventional spin echo condition of readout gradient moment nulling to avoid signal dephasing, although the readout gradient strength varies with slice position. This is achieved by adapting the prephase gradient moment of the standard spin echo sequence for each slice to allow for a rephased signal at $t = TE$.

- Transaxial FoV extension to 600 mm.

The regions to be optimized, i.e. the patient’s arm positions, were automatically determined from the user’s slice positioning. The field parameters were read from a file containing input coefficients based on the measurements described above. The B_0 inhomogeneities and the readout gradient nonlinearities were calculated for each optimization region and each slice position using spherical harmonic field expansion (Eq. 2.8). The optimal readout gradient amplitudes were calculated according to (Eq. 3.5) and adjusted automatically. No further user interaction was needed. In whole-body measurements, the sequence protocol was set to be run in multi-bed stations mode to achieve best possible FoV coverage in z-direction. The patient’s arms can be acquired entirely in length by three bed positions of 25 cm each (neck, thorax and abdomen) and thus the measurement can be integrated in the typical MR-PET workflow. Each slice position was measured twice using the optimal readout gradient amplitude for the left and the right patient’s arm, respectively. The acquisition time was 43 sec per arm position (left/right) for each bed position, 11 slices of 5 mm and 20 mm spacing, TR = 400 ms, FoV = 600 mm, phase-encode FoV = 210 mm, matrix = 320 * 96.

4.2.2 Sequence Design 2: Bipolar Dual Echo Spin-Echo

A dual-echo SE sequence was modified to handle RO gradients with different polarity and amplitude (FIG. 4.2A). An additional prephase moment ensures the spin echo condition for the second echo. The readout gradients have been adapted to acquire a distortion-reduced transaxial slice of the right patient’s arm in the first echo and of the left patient’s arm in the second echo. The optimal space-depending RO gradients were calculated automatically by the sequence according to (Eq. 3.5).

A volunteer experiment was performed on a 3T whole-body system, and a transversal slice at $z = 0$ was acquired. The field-of-view was set to 600 mm with $1.18 * 1.18 \text{ mm}^2$ in-plane resolution and 5 mm slice thickness.

4.2.3 Sequence Design 3: Continuous Table Movement

An optimal readout gradient corresponding to zero distortion was calculated for the right volunteer’s arm position and the left volunteer’s arm position at slice position $z = 0$ (iso-center). A half-Fourier single-shot turbo spin-echo (HASTE) sequence was modified to continuously slide the volunteer through the optimized slice at an off-center position during measurement using continuous table movement (CTM). In a volunteer experiment transversal slices at an off-center position ($x = -300 \text{ mm}$) were acquired during continuous table movement

using a non-optimized readout gradient and an optimized readout gradient. The transaxial FoV was set to 500 mm with $1.95 \times 1.95 \text{ mm}^2$ in-plane resolution and 5 mm slice thickness. The total FoV in z-direction was set to 705 mm.

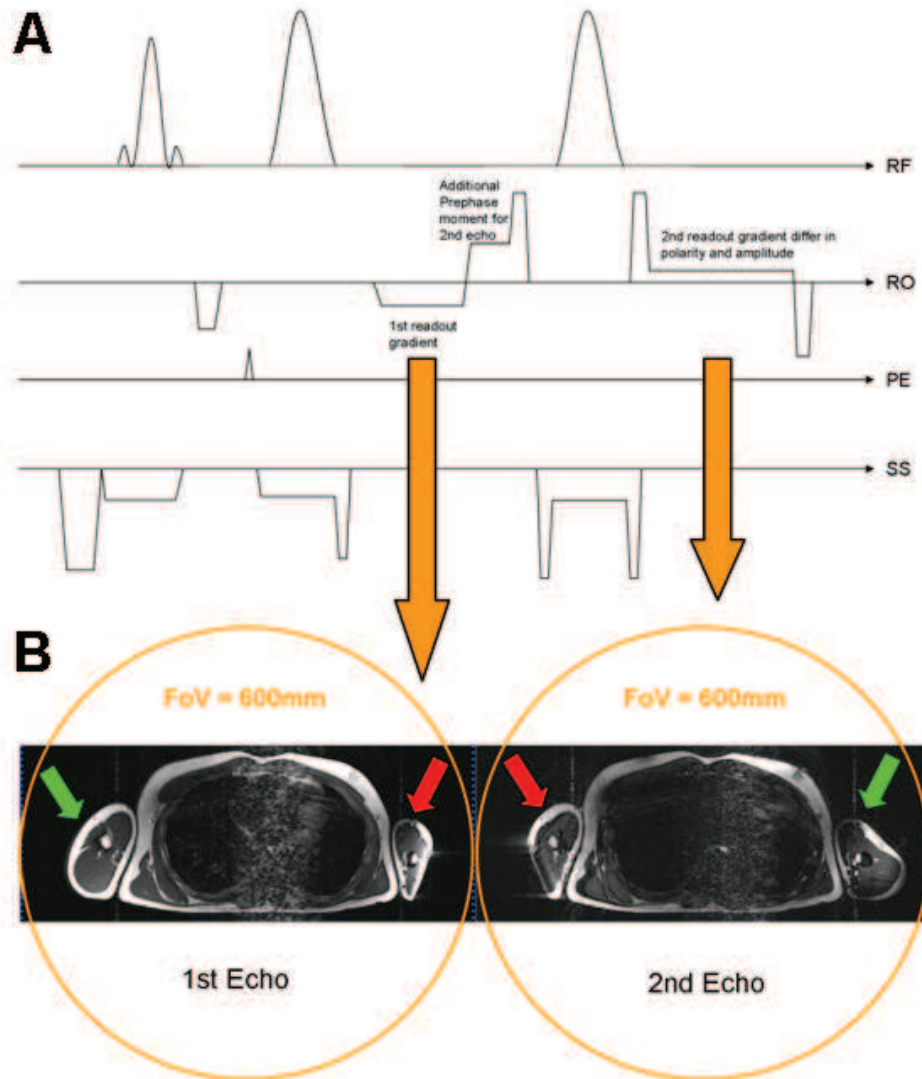


Figure 4.2: Diagram of bipolar dual-echo SE sequence with optimized readout gradients (A) and corresponding echoes of a transversal slice (B). 1st echo: gradient optimization for the right volunteer's arm, 2nd echo: gradient optimization for the left volunteer's arm (green arrows)

4.3 Results

4.3.1 Multi-Slice Spin-Echo-Based Implementation

A significant distortion reduction was achieved at multiple slice positions. Figure 4.3 shows transversal slices at ($z = [-100 \text{ mm}, -80 \text{ mm}, -60 \text{ mm}, -40 \text{ mm}]$) with and without adapting the gradient amplitude for each slice position and for both arm positions (left/right). While the standard spin-echo-based sequence produced strong distortions at the patient's arms resting along the body, the automatic and position-dependent adjustment of the gradient amplitude allowed for a faithful spatial-encoding.

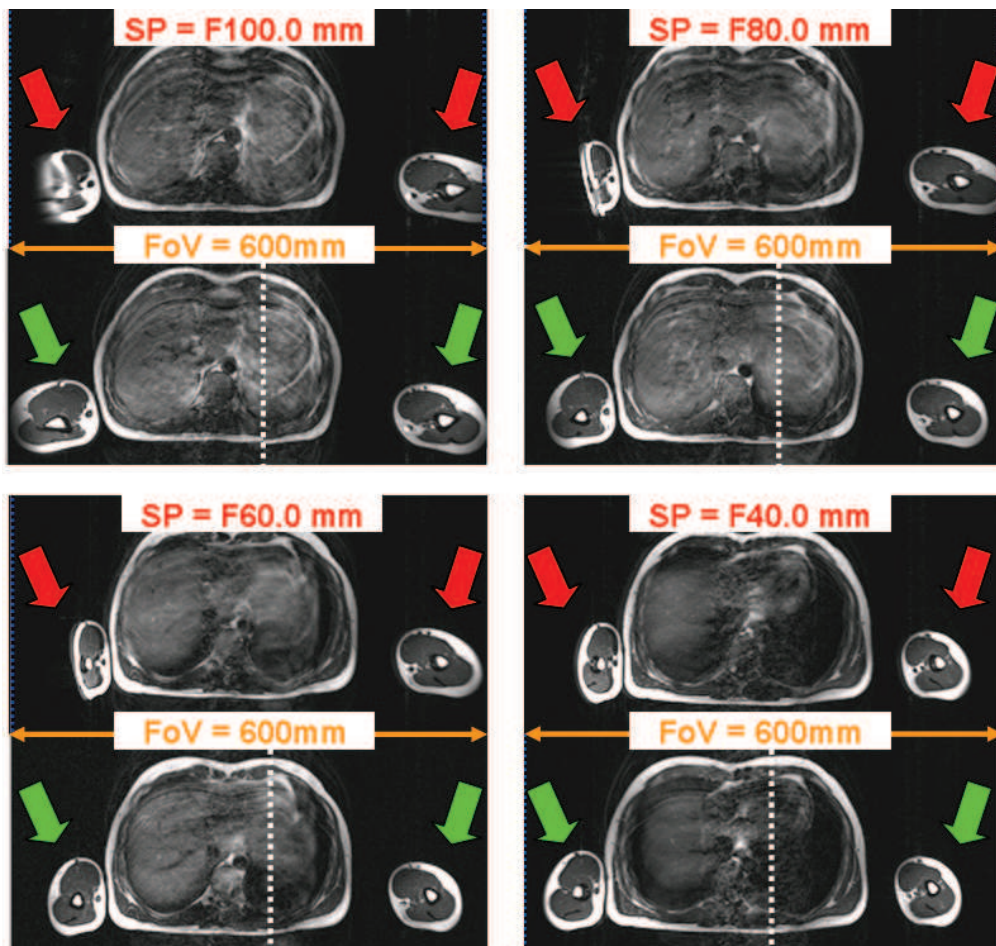


Figure 4.3: Transversal slices acquired at different z -positions. Distortions at off-center positions (red arrows) can be reduced by using the proposed optimization method at multiple slice positions (green arrows).

4.3.2 Bipolar Dual Echo Implementation

A distortion reduction of both the volunteer's left arm and the volunteer's right arm was achieved during one single measurement scan using a bipolar dual echo acquisition with optimized RO gradients. Figure 4.2B shows the acquired images. In the first echo, the right volunteer's arm was imaged nearly faithfully without any post-processing correction, whereas the left volunteer's arm was strongly distorted. This distortion of the left volunteer's arm was minimized in the second echo.

4.3.3 Continuous Table Movement

The volunteer's arms resting along the body were imaged entirely in length. Figure 4.4 shows the off-center measurement using continuous table movement (CTM). The measurement was performed with and without the use of an optimal gradient amplitude at position $z = 0$. In the non-optimized case, a large proportion of the right volunteer's arm was truncated due to strong distortions (Fig. 4.4A). This distortion was significantly reduced using a readout gradient amplitude optimized as proposed (Fig. 4.4B). The data were acquired without spacing between the slices. Thus, no interpolation was required. Consequently, the magnitude of distortion did not vary with slice position.

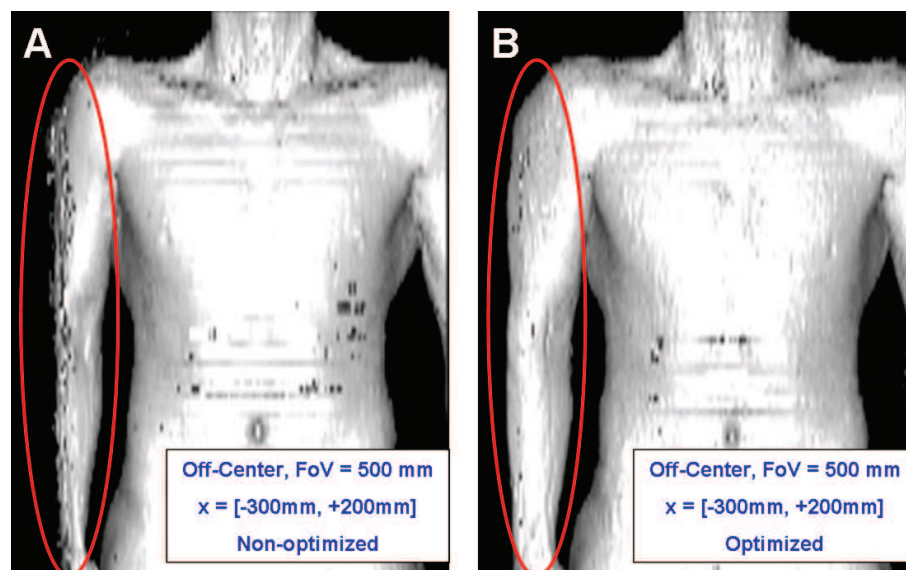


Figure 4.4: 3D shaded surface display of volunteer measured with an transaxial oriented HASTE sequence using continuous table movement. Distortions and signal voids at off-center positions (A) can be reduced using an optimized readout gradient (B).

4.4 Discussion

As shown in chapter 3 the optimal gradient amplitude corresponding to zero-distortion is space-dependent and thus varies with slice position and patient's arm position. The multi-slice spin-echo-based implementation analyzed in this chapter allowed for an inline computation and application of the gradient amplitude optimized for each slice position. An in-plane distortion reduction in the frequency-encoding direction was achieved at several slice positions. However, each slice has to be acquired twice to optimize for both the left and the right patient's arm position.

The two-fold measurement of the same slice can be avoided by implementing a dual-echo SE-based sequence. Dual-echo SE imaging with automatically optimized readout gradients extended the transaxial FoV simultaneously in positive and negative frequency-encoding direction.

Both the variation of the magnitude of distortion with slice-position and the need of interpolation between these slices became obsolete with the use of continuous table movement. Truncation artifacts of the volunteer's arm were reduced by sliding the volunteer through the optimized slice. Therefore, a whole-body acquisition of the complete anatomy with an transaxial FoV of up to 600 mm and an arbitrary total FoV in table moving direction can be acquired. The proposed method of an transaxial FoV extension using an optimized readout gradient field combined with continuous table movement significantly reduced typical truncation artifacts at off-center positions. From a workflow perspective, this method could optimally be combined with a PET acquisition using continuous table movement [7].

4.5 Conclusion

Distortion reductions can be achieved in multiple slices. An automatic optimization of the gradient amplitude was achieved for each slice position. The optimization of both the left and the right patient's arm in the same excitation train is feasible with the bipolar dual-echo approach. Continuous table movement allows for a full coverage of the patient's arm with minimal residual distortion and without the need of interpolation.

In summary, the proposed distortion reduction method became feasible for clinical use.

References

- [1] Bornert P, Aldefeld B. Principles of whole-body continuously-moving-table MRI. *J Magn Reson Imaging* 2008;28(1):1–12.

- [2] Zenge MO, Ladd ME, Quick HH. Novel reconstruction method for three-dimensional axial continuously moving table whole-body magnetic resonance imaging featuring autocalibrated parallel imaging GRAPPA. *Magn Reson Med* 2009;61(4):867–873.
- [3] Zenge MO, Ladd ME, Vogt FM, Brauck K, Barkhausen J, Quick HH. Whole-body magnetic resonance imaging featuring moving table continuous data acquisition with high-precision position feedback. *Magn Reson Med* 2005;54(3):707–711.
- [4] Zenge MO, Vogt FM, Brauck K, Jokel M, Barkhausen J, Kannengiesser S, Ladd ME, Quick HH. High-resolution continuously acquired peripheral MR angiography featuring partial parallel imaging GRAPPA. *Magn Reson Med* 2006;56(4):859–865.
- [5] Polzin JA, Kruger DG, Gurr DH, Brittain JH, Riederer SJ. Correction for gradient nonlinearity in continuously moving table MR imaging. *Magn Reson Med* 2004;52(1):181–187.
- [6] Blumhagen JO, Ladebeck R, Fenchel M, Scheffler K. Multislice 2D spin echo imaging using adapted readout gradients for compensation of BO inhomogeneities and gradient nonlinearities. In *Proceedings of the 28th Annual Meeting of ESMRMB, Leipzig, Germany, 2011*. p. 604.
- [7] Braun H, Ziegler S, Paulus DH, Quick HH. Hybrid PET/MRI imaging with continuous table motion. *Med Phys* 2012;39(5):2735–2745.

Chapter 5

Clinical Application and Patient Study: Impact on Quantitative PET Reconstruction

5.1 Introduction

As described in chapter 1, the attenuation correction of the PET emission data is essential for PET quantification. In PET/CT the linear attenuation coefficients (LAC) can directly be converted from the low-dose CT image to AC maps at 511 keV [1]. In MR/PET the LACs cannot be obtained from the MR image in the same way due to the fact that the MR contrast is independent of the electron density of the tissue and thus contains no direct information about the photon attenuation magnitude. A segmentation approach [2] in four tissue compartments (air: 0 cm^{-1} , lung: 0.018 cm^{-1} , fat: 0.086 cm^{-1} and soft-tissue: 0.10 cm^{-1}) based on a 2-point DIXON sequence [3, 4] is promising and results in acceptable biases of standardized uptake values (SUV). Residual deviations of the SUV can be explained by several causes [5]. The contribution of bone tissue is ignored in current approaches where bone is treated as soft-tissue. The radiofrequency (RF) surface coils contribute to the photon attenuation but are typically not accounted for in the attenuation model [6]. Finally, the MR field-of-view (FoV) is limited due to physical restrictions. Consequently, truncation artifacts occur at the edges of the FoV in the AC map and thus the PET reconstruction can potentially be biased [7]. For the modeling of bone tissue, an atlas-based approach was proposed by Hofmann et al. [8]. An alternative approach for bone segmentation was achieved by dedicated MR sequences using ultrashort echo times [9]. The MR hardware inside the PET FoV, particularly the surface coils and the patient table, can be manufactured of less attenuating components, or, preferably, attenuating components can be placed outside the PET FoV. The attenuation correction of residual hardware is done by considering the position and the attenuation coefficients of each hardware component [10, 11]. For completion of the truncated attenuation map, Nuyts et al. showed the feasibility of the prediction of the missing body contour from the attenuation PET emission data using a maximum-likelihood a-posteriori algorithm (MLAA) [12]. However, this approach requires additional calculation time and relies on sufficient radioactive tracer uptake in the truncated parts such as the arms and the skin to successfully derive accurate data from the PET emission data. Against this backdrop, in chapter 3 it has been shown that by considering the actual field plots of a specific MR/PET hybrid imager, space-dependent optimal readout gradients can be found which compensate the distortion due to the inhomogeneity of the main magnetic field and the distortion due to the non-linearity of the gradient field [13].

In this chapter, we will show a purely MR-based method for completion of truncated AC maps in MR/PET hybrid imaging. In conventional MR Fourier-transform imaging, proper spatial encoding requires a homogeneous main magnetic field and linear gradient fields. These conditions are fulfilled for typical FoV volumes within the specified imaging FoV. At off-center positions inhomogeneities of the main magnetic field and gradient nonlinearities cause geometri-

cal distortions of body regions located outside the specified FoV. These regions often include the patient's arms [14–16]. The distortions cause truncations in the MR-based AC map and might hamper an accurate attenuation correction in MR/PET hybrid imaging [7]. A complete non-truncated AC map for the attenuating body tissue on the pathway of the 511 keV photons, however, is important for exact attenuation correction and for the modeling and scaling of scatter [17–22].

In this work, the MR-based FoV extension technique was used to complete the truncated AC maps. Furthermore, the impact of the FoV extension technique on the PET quantification was analyzed. The extended AC maps were acquired for 12 patients who underwent an ^{18}F -FDG PET/CT and subsequently an MR/PET examination. Retrospective ordinary Poisson ordered-subsets expectation-maximization (OP-OSEM) reconstructions (3 iterations, 21 subsets) of the PET data were performed using the conventional and the extended MR-based AC maps. Quantitative comparisons of the attenuation corrected PET reconstructions were conducted with the PET/CT scans of the same patients as an intraindividual standard of reference.

5.2 Materials and Methods

Towards the aim to improve the MR-based attenuation correction of the PET emission data, a spin-echo MR sequence was developed to reduce typical truncation artifacts in the MR image due to FoV limitations. First, the conventional DIXON-based AC map was measured. Then, additional MR acquisitions were performed at bi-lateral off-center positions using the MR-based FoV extension. The patient's arms were segmented based on the distortion-reduced image. Finally, this additional segmentation result was used to complete the truncated AC map (Fig. 5.1).

Simultaneous MR/PET scanning was performed on an integrated MR/PET hybrid whole-body imaging system (Biograph mMR, Siemens AG Healthcare Sector, Erlangen, Germany) at the Institute of Medical Physics, University of Erlangen-Nuremberg, Germany. The intraindividual PET/CT comparison scans were performed on a whole-body PET/CT scanner (Biograph mCT 64, Siemens AG Healthcare Sector, Erlangen, Germany) at the University Hospital Erlangen, Germany.

5.2.1 MR-based FoV Extension

Geometrical distortions at the edges of an extended FoV due to B_0 inhomogeneities and gradient nonlinearities were compensated by using an optimal readout gradient as it has been described in chapter 3. The optimal readout

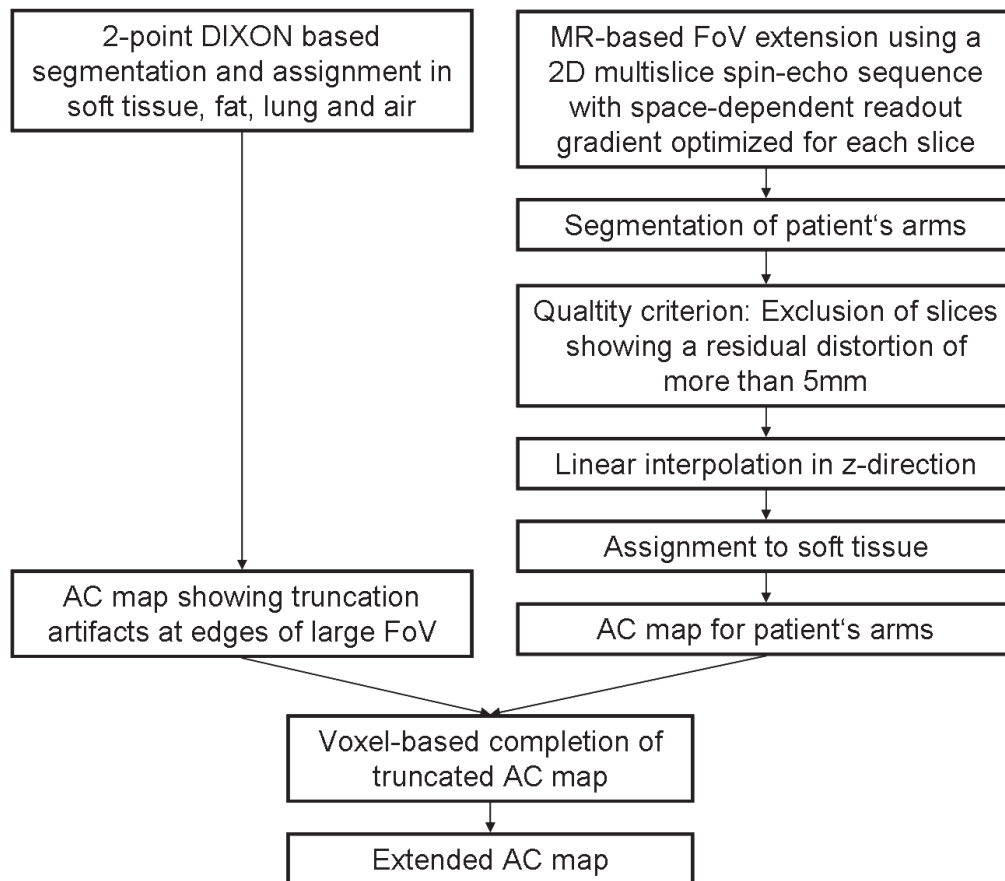


Figure 5.1: Flow chart depicting main steps involved in reducing truncation artifacts of the AC map.

gradient corresponding to zero-distortion is space-dependent and might differ for every voxel-position according to Eq. 3.5. However, it was shown that the use of a single optimal readout gradient for each patient arm and each slice position was sufficient to achieve a significant in-plane distortion reduction where the patient's arms are resting besides the body during the MR/PET examination. The system-specific B_0 inhomogeneities of the main magnet field and the nonlinearities of the gradient field were measured once using an MR probe device as described in chapter 2.

A multislice 2D spin-echo-based sequence was implemented to determine and automatically apply the optimal gradient strength depending on the slice position [23]. No hardware changes or user interactions were required. The measurement of the patient's arms over their entire length was separated into multiple bed stations. Each slice position was measured twice using the optimal readout gradient amplitude for the left and the right patient arm, respectively. The acquisition time was 43 s per arm position (left/right) for each bed position. Usually three or four bed stations are required for whole arm coverage. At each bed position, 11 transaxial slices of 5 mm and 20 mm spacing were acquired, TR = 400 ms, frequency-encode FoV = 600 mm, phase-encode FoV = 210 mm, matrix = 320 * 96.

Using the optimal readout gradient, the distortion can usually be reduced significantly for the center slice at $z = 0$ mm of each bed station but off-center slices might show residual distortion. Thus, slices showing a distortion of more than 5 mm compared to the center-slice were automatically excluded from further post-processing. Assuming a homogeneous structure of the patient's arm in the z -direction, a linear interpolation between the non-excluded slices was performed.

5.2.2 AC Map Completion

The conventional AC map was generated based on a 2-point DIXON technique, which allows for segmentation into four tissue classes (soft-tissue, fat, lung and air). The MR measurement was performed at three or four bed positions (head, thorax, abdomen, and pelvis) and resulted in a composed AC map with a resolution of $2.6 * 2.6 * 2.6$ mm³ and up to $500 * 330 * 922$ mm³ in volume coverage. The extension of the AC map in the transaxial direction was performed using Matlab R2010b (The MathWorks, Inc., Natick, MA, USA). The MR images acquired in the extended FoV as described above were used to build a binary mask containing the patient's arms (Fig. 5.2). The pixels in the mask were assigned to the AC values of soft-tissue ($\mu = 0.1$ cm⁻¹) and air ($\mu = 0$ cm⁻¹) for the patient's arms and the background, respectively. A pixel-wise completion of the AC map was performed based on this mask where each pixel at the edge region (20 cm $< |x| < 30$ cm) of the original AC map which was potentially misassigned to background due to truncation artifacts was reassigned to the

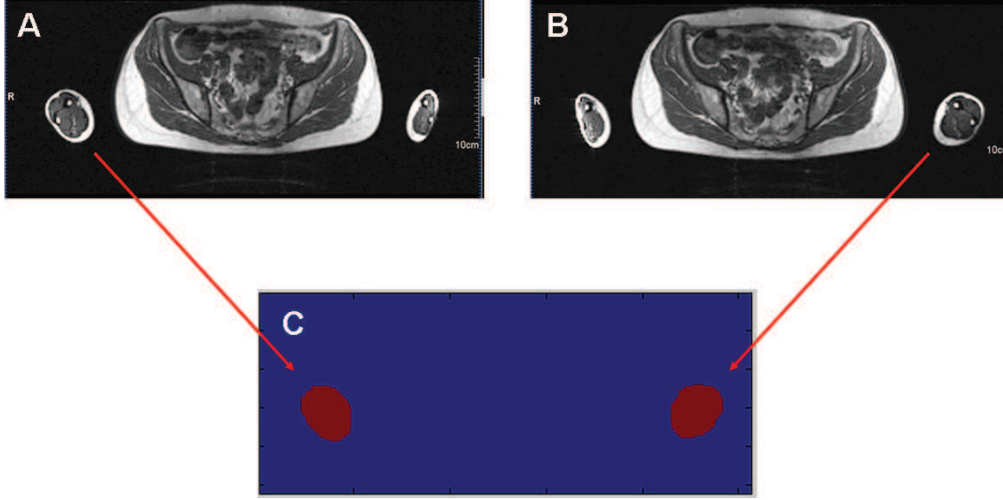


Figure 5.2: Distortion-reduced off-center acquisition and segmentation. Transaxial slices acquired using the proposed FoV extension technique optimized for the right patient's arm (A) and the left patient's arm (B) were used for generating a binary mask (C) after segmentation of patient's arms.

corresponding mask's pixel value. The resolution of the MR data acquired in the extended FoV was sufficient for a pixel-wise completion of the AC in the x- and y-direction. However, the resolution in the z-direction was limited by the number of slices to reduce acquisition time. Thus, a linear interpolation of the binary mask was performed in the z-direction to achieve the same resolution as in the original AC map.

5.2.3 Impact on the PET Reconstruction

For validating the improvement and the impact of the proposed MR-based FoV extension of the AC map on the PET reconstruction, 12 patients who underwent a ^{18}F -FDG PET/CT and subsequently a simultaneous MR/PET examination were measured using the described imaging technique.

The extended and the original (distorted) AC maps were used for retrospective ordinary Poisson ordered-subsets expectation-maximization (OP-OSEM) reconstructions [24] with 3 iterations, 21 subsets; Gaussian filter FWHM 4 mm.

The body weight corrected standardized uptake values (SUV_{bw}) were calculated as

$$SUV_{bw} = \frac{C_{PET}}{D_{PET}/BW}, \quad (5.1)$$

where C_{PET} is the tissue radioactivity concentration, D_{PET} is the injected dose and BW is the patient's body weight.

To quantify the impact of the proposed method on the PET reconstruction,

first the SUV_{mean} values were compared in three spine lesions with those of the CT-based PET reconstruction in one patient. Afterwards, an inter-patient comparison of the different attenuation correction approaches was performed in two three-dimensional regions of interest (ROIs) placed at the image position of the liver and the spine of 12 patients respectively. To verify the potential improvement of the quantitative PET reconstruction using our approach, a CT-based AC PET reconstruction was performed and compared to the MR-based AC PET reconstructions with and without extended FoV. Assuming a higher impact of the FoV extension method for obese patients the quantitative comparison was performed on the patient with the largest body mass index (BMI: 33.60 kg/m^2). The patient showed several osseous metastases. Three ROIs were placed at spine lesions showing a mean $SUV_{bw} > 5$ and used for comparison between the MR-based AC PET reconstructions (Fig. 5.3) and the CT-based AC PET reconstruction. To validate the impact of the proposed method, an inter-

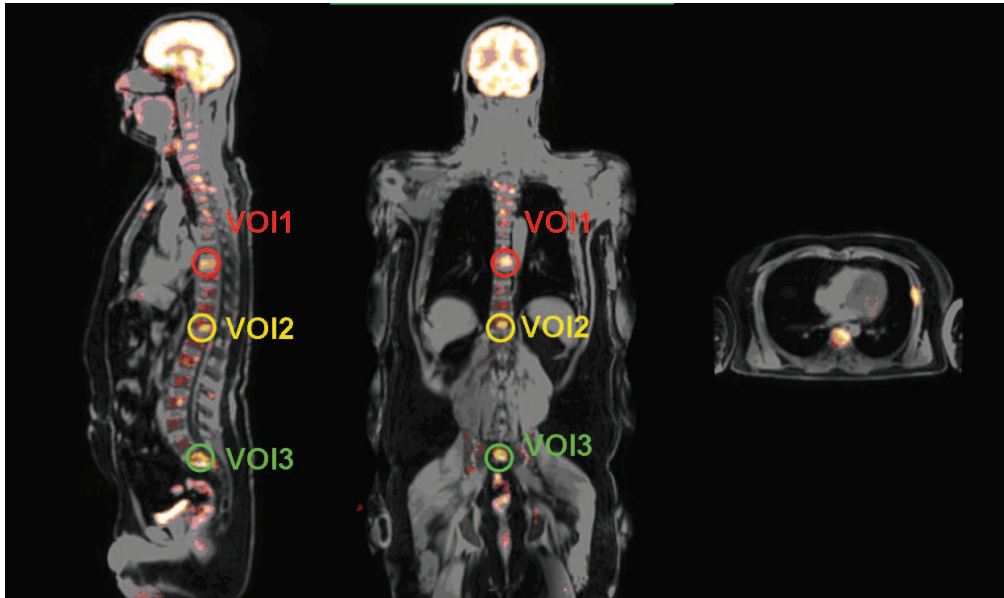


Figure 5.3: MR/PET hybrid imaging of a patient with tracer active bone lesions in sagittal (left), coronal (middle), and transaxial (right) orientation. Three spine lesions were defined for intraindividual quantitative comparison between MR-based attenuation correction with and without extended FoV and CT-based attenuation correction.

patient study was performed comparing the MR-based AC PET reconstructions with and without extended FoV in 12 patients. Furthermore, the purely MR-based AC extension was compared to the PET-based truncation completion of the body contour by the MLAA algorithm [12]. Three-dimensional ROIs were placed in the liver and in the thoracic spine (Fig. 5.4). The position and the

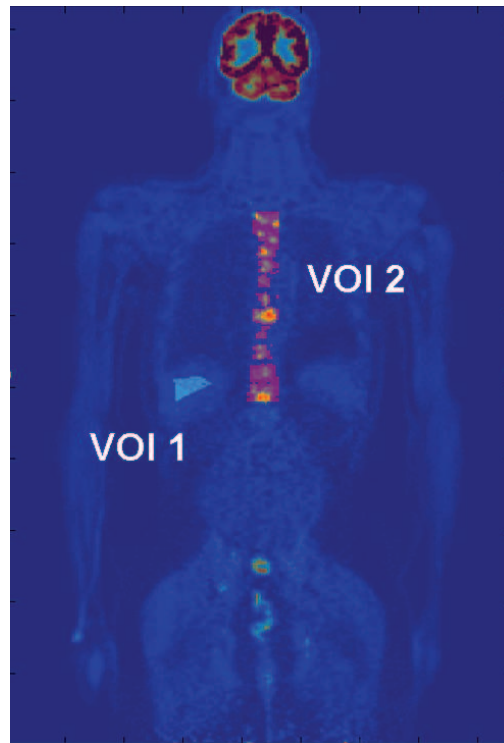


Figure 5.4: Coronal slice of PET reconstruction. Colored volumes (blue and red) depict the defined three-dimensional regions of interest in the liver (VOI 1) and the thoracic spine (VOI 2) used for the inter-patient comparison of the impact of the proposed MR FoV extension on the PET quantification. Only voxels showing a $SUV_{bw} > 1$ were included.

size of the ROIs were the same for the different PET reconstructions in each patient but differed due to inter-patient anatomical variance.

5.2.4 Patient Population

This study involved 12 patients (6 male, 6 female, BMI: $23.91 \text{ kg/m}^2 \pm 5.35 \text{ kg/m}^2$) of the University Hospital Erlangen, Germany. Only patients who underwent a PET/CT scan after clinical indications were examined in MR/PET. Thus, the PET tracer was injected only once and additional radiation exposure was avoided. The study was IRB approved by the local ethics committee. Written informed consent was obtained from all patients before imaging.

5.3 Results

The proposed MR-based FoV extension achieved an improvement of the AC map in all patients. Figure 5.5 shows the AC map before and after the described technique. Typical truncation artifacts of the patient’s arms (Fig. 5.5A) due to

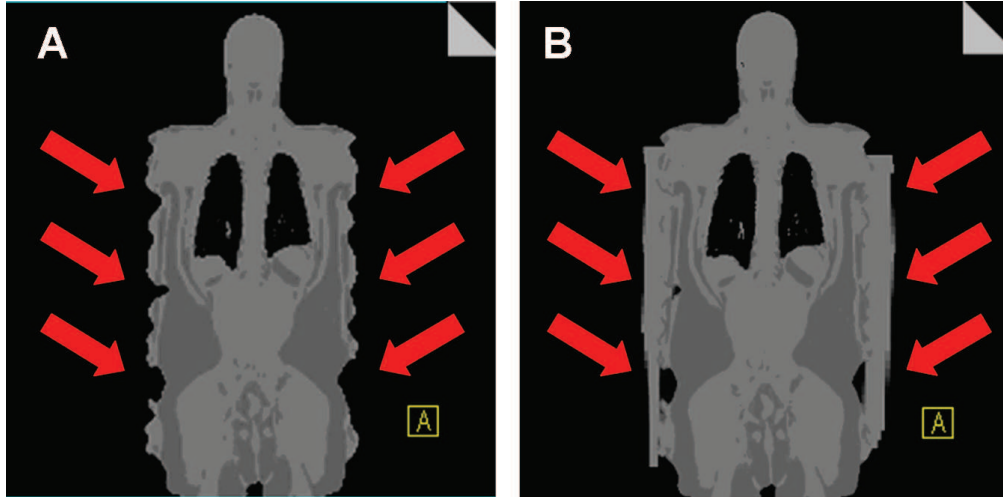


Figure 5.5: Attenuation correction map without (A) and with the proposed FoV extension (B). The typical truncation artifacts (red arrows) were significantly reduced.

FoV limitations were significantly reduced (Fig. 5.5B). Average body volume increased by $5.08 \% \pm 1.94 \%$ in the AC map with total average body volume coverage of 49.18 dm^3 for the limited FoV and 51.88 dm^3 for the extended FoV. The resulting PET reconstructions are shown in Figure 5.6. The PET reconstruction processed by the conventional MR-based AC without FoV extension (Fig. 5.6A) showed a signal underestimation of both the patient’s arms and of several spine lesions when compared to the PET reconstructions processed by the proposed FoV extension (Fig. 5.6B) and by the MLAA algorithm (Fig. 5.6C). Figure 5.7 shows the voxel-wise change of SUV_{bw} values in the PET reconstructions using the HUGE technique (Fig. 5.7A) and the MLAA algorithm (Fig. 5.7B) each in relation to the AC without FoV extension. The largest bias compared to the limited FoV was found in the patient’s arms and in the thoracic spine for both HUGE and MLAA. The comparison of the PET reconstructions using the MR-based FoV extension HUGE, the PET-based FoV extension MLAA and the CT-based attenuation correction was quantified in three spine lesions and is shown in absolute SUV_{bw} mean values and in percentage deviation from the limited FoV AC PET reconstruction in Table 5.1. The standard deviations of all three-dimensional ROIs were between 1.49 and 2.97. The largest deviation between the MR-AC PET reconstruction without FoV exten-

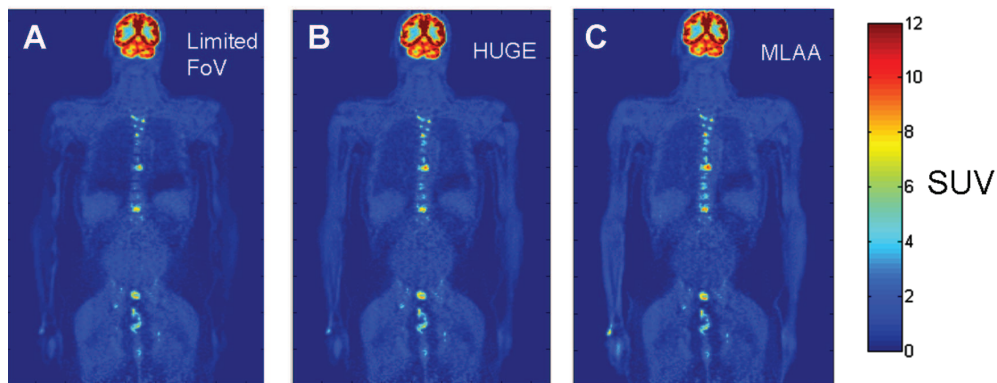


Figure 5.6: PET reconstructions processed by MR-AC without any FoV extension algorithms (A), with the proposed MR-based FoV extension (B) and with an extension by PET-based estimation (C). Note the better PET visibility of the corrected arms in (B) and (C) and associated higher lesion activity for the spine lesions.

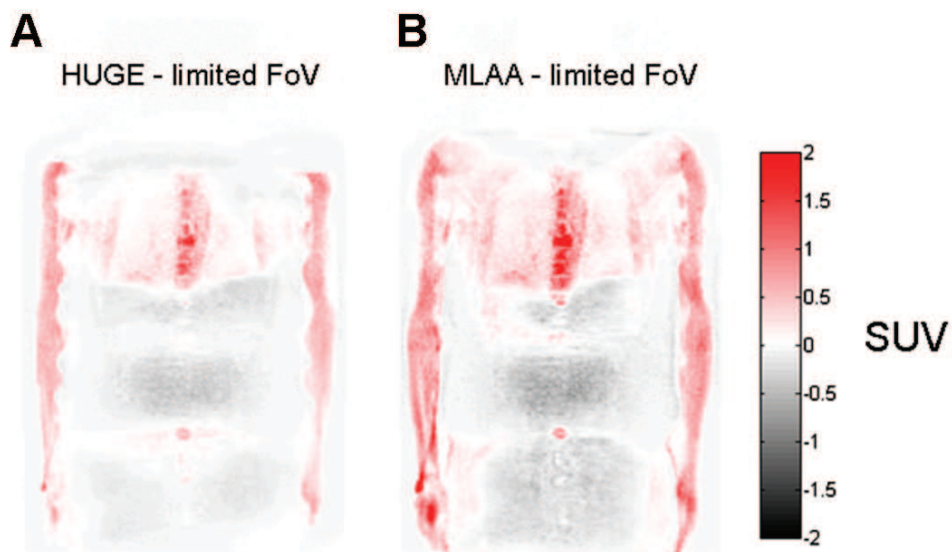


Figure 5.7: Voxel-based bias of PET reconstructions using MR-AC with proposed FoV extension (A) and PET-based completion estimation (B) compared to MR-AC without any FoV extension algorithms. Note the identical regions of bias in the arms and the thoracic spine.

Spine Lesions	MR-based AC with no FoV extension	MR-based AC with MR-based FoV extension	MR-based AC with PET-based FoV extension	CT-based AC
<u>VOI 1</u> SUV_{mean} : Deviation from limited FoV:	5.29 n.a.	6.52 23.25%	7.53 42.34%	7.08 33.84%
<u>VOI 2</u> SUV_{mean} : Deviation from limited FoV:	6.14 n.a.	6.07 -1.14%	6.34 3.26%	6.24 1.63%
<u>VOI 3</u> SUV_{mean} : Deviation from limited FoV:	6.63 n.a.	6.93 4.52%	6.70 1.06%	7.30 10.11%

Table 5.1: Quantitative comparison of PET reconstructions processed by different MR-based AC algorithms and CT-based AC performed in three spine lesions and given in SUV_{mean} and percentage deviation from MR-based AC using normal specified FoV. Standard deviations within defined regions-of-interest varied from 1.49 to 2.97. Three-dimensional VOIs were positioned as shown in Fig. 5.3.

	MR-based AC with MR-based FoV extension (HUGE)	MR-based AC with PET-based FoV extension (MLAA)
<u>VOI 1 (Liver)</u>		
Mean $\mu \pm$ Std σ :	$-0.05\% \pm 5.44\%$	$-0.03\% \pm 6.75\%$
<u>VOI 2 (Spine)</u>		
Mean $\mu \pm$ Std σ :	$6.19\% \pm 4.12\%$	$14.74\% \pm 8.54\%$

Table 5.2: Comparison of PET quantification using the MR-based AC with proposed MR-based FoV extension and MR-based AC with PET-based FoV completion. Values are given in percentage deviation from MR-based AC without FoV extension. The three-dimensional VOIs were drawn in the liver and in the thoracic spine of 12 patients as shown in Fig. 5.4.

sion and with FoV extension was found in ROI1 with a higher SUV_{bw} value of 23.25 % using HUGE ($SUV_{bw,HUGE,ROI1} = 6.52$, $SUV_{bw,limitedFoV,ROI1} = 5.29$). In comparison to the CT-based AC PET reconstruction ($SUV_{bw,PET/CT,ROI1} = 7.08$), the AC using HUGE underestimated the PET reconstruction by 7.91 % and MLAA overestimated the PET reconstruction by 6.36 % in ROI 1. ROI 2 showed the smallest deviation with -1.14 % using HUGE ($SUV_{bw,HUGE,ROI2} = 6.07$, $SUV_{bw,limitedFoV,ROI2} = 6.14$). In relation to the CT-based AC PET reconstruction using HUGE underestimated the PET quantification by 2.72 % ($SUV_{bw,HUGE,ROI2} = 6.07$) and MLAA overestimated the PET reconstruction by 1.60 % ($SUV_{bw,MLAA,ROI2} = 6.34$) in ROI 2. ROI 3 showed a deviation of 4.52 % using HUGE ($SUV_{bw,HUGE,ROI3} = 6.93$) compared to using the limited FoV ($SUV_{bw,limitedFoV,ROI3} = 6.63$). In comparison to the CT-based AC PET reconstruction with HUGE underestimated the PET quantification by 5.07 % ($SUV_{bw,HUGE,ROI3} = 6.93$) and MLAA underestimated the PET reconstruction by 8.22 % ($SUV_{bw,MLAA,ROI3} = 6.70$) in ROI 3.

The inter-patient comparison of the impact of the MR-based attenuation corrected with limited FoV, HUGE and MLAA on the PET reconstruction quantified in the liver and the thoracic spine in 12 patients is shown in Table 5.2. While the deviation of the mean SUV_{bw} using the extended FoV for the AC compared to the limited FoV was small in the liver both using HUGE ($\Delta_{HUGE,liver} = -0.05\% \pm 5.44\%$) and using MLAA ($\Delta_{MLAA,liver} = -0.03\% \pm 6.75\%$), it

was considerably large in the thoracic spine ($\Delta_{HUGE,spine} = 6.19 \% \pm 4.12 \%$, $\Delta_{MLAA,spine} = 14.74 \% \pm 8.54 \%$).

5.4 Discussion

The proposed MR-based FoV extension technique reduced significantly the typical truncation artifacts in the MR-based attenuation correction maps. The AC maps represent the given patient anatomy more correctly. The average body volume coverage increased by 5.08 % in 12 patients due to the FoV extension technique. The AC map completed with the MR-based FoV extension improved the MR-based attenuation correction and thus the PET quantification in MR/PET hybrid imaging.

The inter-patient study showed that the impact of HUGE and MLAA on the PET reconstruction depends on the body region. While the mean percentage deviation in the liver was insignificant with -0.05 % and -0.03 % using HUGE and MLAA, respectively, the impact was remarkable in the thoracic spine with 6.19 % and 14.74 %. This can potentially be explained by the fact that the lungs have a 5 times lower attenuation factor than soft-tissue and thus increase the proportionate impact of the patient's arms on the attenuation correction in the thorax relative to the abdomen. The standard deviation of the stated impact with up to 5.44 % for HUGE and 8.54 % for MLAA and the standard deviation of the additional volume used for completion of the AC map with 1.94 % indicates that the potential improvement of an extended AC map is highly patient-dependent. Both the amount of additional volume required for filling the truncations and the positions of truncation artifacts in the AC map differs for different patients and thus causes the observed variance in the impact on PET quantification.

To verify that the observed impact also successfully causes an improvement of the PET quantification, an intraindividual comparison to the PET/CT examination was performed exemplarily in the patient with the largest impact of the FoV extension. Here, the PET/CT scan cannot be treated as a gold-standard for the MR/PET quantification due to several aspects. Pharmacokinetic factors, such as enhancement and washout over time due to different time intervals between injection time and start of the PET study (97 min p.i. for PET/CT and 184 min p.i. for MR/PET), biological factors, such as patient motion and patient exercise due to transport from one modality to the other, and physical factors, such as ROI definition, might hamper an accurate quantitative intraindividual comparison between the MR/PET and the PET/CT examination [25–28]. Therefore, the comparison to PET/CT did not aim at a quantitative agreement but was performed in one patient to show the reduced bias of the proposed technique. The lesion-dependent bias between MR-based AC PET and PET/CT was reduced to a maximum percentage deviation of 7.9 % by extending

the MR FoV using HUGE. The comparison between the PET reconstructions processed by MR-based attenuation correction algorithms and by a CT-based attenuation correction validated that the observed impact improves the PET quantification. Furthermore, medical experts have stated that a maximum bias of 10 % with respect to PET/CT is acceptable for MR-based attenuation correction [5]. Thus, the residual bias typically does not affect diagnosis except as part of several systematic errors that could sum up.

In comparison to the PET-based AC map completion using the MLAA algorithm, the proposed technique is purely MR-based and thus independent of the choice of radiotracer. While MLAA works best using radiotracers with sufficient background uptake for computation of the body contour [7], the MR-based FoV extension works also in case of little uptake in the patient's arms. Furthermore, the MR-based approach did not require additional computation time as MLAA. On the other hand, the MLAA algorithm could, in theory, be extended to obtain attenuation values of the surface coils with medium to low attenuation coefficients [12], which cannot be imaged by the purely MR-based attenuation correction. Theoretically, the MR-based and the PET-based AC map completion can be combined such that the additional distortion-reduced MR data is used as initial input for a faster and more accurate iterative calculation from the PET emission data using MLAA.

While the DIXON-technique allows for segmentation in different tissue classes, the proposed FoV extension technique in its current implementation assigns all voxels of the truncated patient's arms to soft-tissue. Thus, an additional fat-water separation of the MR data acquired outside the specified FoV might cause further improvement. However, a combination of the DIXON-technique and the dedicated MR sequence for the distortion-free acquisition might be challenging with respect to increasing measurement time and phase correction issues. Nevertheless, the image contrast of the acquired patient's arms (Fig. 5.2) already seems promising for a histogram-based grayscale segmentation of fat [29], which will be subject to further research.

The presented multislice spin-echo-based sequence implementation using optimal readout gradients for each slice position achieved a significant overall distortion reduction. However, the residual distortion varied with the slice position. As mentioned, slices with a residual distortion of more than 5 mm were excluded from further post-processing and linear interpolation was performed instead. A further improvement might be a sequence implementation using continuous table movement [30]. The data with such an approach is acquired only at the slice position showing no residual distortion and the patient table moves the patient through this slice. This modification is still a subject for further research but initial results are promising [31, 32].

5.5 Conclusion

The proposed technique successfully extends the MR FoV in MR-based attenuation correction and recovers the truncated body parts in the AC map. The use of this completed AC map shows an improvement of PET quantification in whole-body MR/PET hybrid imaging.

In comparison with PET-based approaches, the presented algorithm is purely MR-based and thus also applicable to specialized PET tracers with little uptake in the arms. Furthermore, the method might also be of interest for dynamic PET acquisitions for special applications such as oncology and cardiology with uptake distributions varying over time.

References

- [1] Kinahan PE, Hasegawa BH, Beyer T. X-ray-based attenuation correction for positron emission tomography/computed tomography scanners. *Semin Nucl Med* 2003;33(3):166–179.
- [2] Martinez-Moeller A, Souvatzoglou M, Delso G, Bundschuh RA, Ched'hotel C, Ziegler SI, Navab N, Schwaiger M, Nekolla SG. Tissue classification as a potential approach for attenuation correction in whole-body PET/MRI: evaluation with PET/CT data. *J. Nucl. Med.* 2009;50(4):520–526.
- [3] Coombs BD, Szumowski J, Coshov W. Two-point Dixon technique for water-fat signal decomposition with B0 inhomogeneity correction. *Magn Reson Med* 1997;38(6):884–889.
- [4] Eiber M, Martinez-Moeller A, Souvatzoglou M, Holzapfel K, Pickhard A, Loffelbein D, Santi I, Rummeny EJ, Ziegler S, Schwaiger M, Nekolla SG, Beer AJ. Value of a Dixon-based MR/PET attenuation correction sequence for the localization and evaluation of PET-positive lesions. *Eur. J. Nucl. Med. Mol. Imaging* 2011;38(9):1691–1701.
- [5] Hofmann M, Pichler B, Scholkopf B, Beyer T. Towards quantitative PET/MRI: a review of MR-based attenuation correction techniques. *Eur. J. Nucl. Med. Mol. Imaging* 2009;36 Suppl 1:93–104.
- [6] Tellmann L, Quick HH, Bockisch A, Herzog H, Beyer T. The effect of MR surface coils on PET quantification in whole-body PET/MR: results from a pseudo-PET/MR phantom study. *Med Phys* 2011;38(5):2795–2805.
- [7] Delso G, Martinez-Moeller A, Bundschuh RA, Nekolla SG, Ziegler SI. The effect of limited MR field of view in MR/PET attenuation correction. *Med Phys* 2010;37:2804–2812.

- [8] Hofmann M, Steinke F, Scheel V, Charpiat G, Farquhar J, Aschoff P, Brady M, Scholkopf B, Pichler BJ. MRI-based attenuation correction for PET/MRI: a novel approach combining pattern recognition and atlas registration. *J. Nucl. Med.* 2008;49:1875–1883.
- [9] M. D. Robson, G. M. Bydder. Clinical ultrashort echo time imaging of bone and other connective tissues. *NMR Biomed* 2006;19(7):765–780.
- [10] Delso G, Martinez-Moeller A, Bundschuh RA, Ladebeck R, Candidus Y, Faul D, Ziegler SI. Evaluation of the attenuation properties of MR equipment for its use in a whole-body PET/MR scanner. *Phys Med Biol* 2010;55:4361–4374.
- [11] Paulus DH, Braun H, Aklan B, Quick HH. Simultaneous PET/MR imaging: MR-based attenuation correction of local radiofrequency surface coils. *Med Phys* 2012 in print.
- [12] Nuyts J, Michel C, Fenchel M, Bal G, Watson G. Completion of a Truncated Attenuation image from the Attenuated PET Emission Data. *IEEE Nucl Sci Symp Conf Record* 2010;oct-nov.
- [13] Blumhagen JO, Ladebeck R, Fenchel M, Kampmeier J, Scheffler K. MR-based Field-of-View Extension: Compensation of Field Imperfections. In *Proceedings of the 19th Annual Meeting of ISMRM, Montreal, Quebec, Canada, 2011.* p. 2693.
- [14] Wang D, Strugnell W, Cowin G, Doddrell DM, Slaughter R. Geometric distortion in clinical MRI systems Part I: evaluation using a 3D phantom. *Magn Reson Imaging* 2004;22(9):1211–1221.
- [15] Dammann P, Kraff O, Wrede KH, Ozkan N, Orzada S, Mueller OM, Sandalcioğlu IE, Sure U, Gizewski ER, Ladd ME, Gasser T. Evaluation of hardware-related geometrical distortion in structural MRI at 7 Tesla for image-guided applications in neurosurgery. *Acad Radiol* 2011;18(7):910–916.
- [16] Baldwin LN, Wachowicz K, Thomas SD, Rivest R, Fallone BG. Characterization, prediction, and correction of geometric distortion in 3 T MR images. *Med Phys* 2007;34:388–399.
- [17] Ollinger JM. Analytic correction for scatter in fully 3D PET: statistical issues. *Nuclear Science Symposium, 1997.* *IEEE* 1997;2:1386–1389.
- [18] Watson CC, Newport D, Casey ME. A single scatter simulation technique for scatter correction in 3D PET. in *Three-Dimensional Image Reconstruction in Radiology and Nuclear Medicine* (P. Grangeat and J-L. Amans, eds.), Dordrecht: Kluwer, 1996.

- [19] Watson CC, Newport D, Casey ME, deKemp RA, Beanlands RS, Schmand M. Evaluation of simulation-based scatter correction for 3-D PET cardiac imaging. *IEEE Trans. Nuc. Sci.* 1997;44:90–97.
- [20] Watson CC. New, faster, image-based scatter correction for 3D PET. *IEEE Trans. Nucl. Sci.* 2000;47:1589–94.
- [21] Watson CC, Casey ME, Michel C, Bendriem B. Advances in scatter correction for 3D PET/CT. *Nuclear Science Symposium Conference Record, 2004 IEEE* 2004;5:3008–3012.
- [22] Thielemans K, Manjeshwar R, Jansen F, Tsoumpas C. A new algorithm for scaling of PET scatter estimates using all coincidence events . *Nuclear Science Symposium Conference Record, 2007 IEEE* 2007;5:3586–3590.
- [23] Blumhagen JO, Ladebeck R, Fenchel M, Scheffler K. Multislice 2D spin echo imaging using adapted readout gradients for compensation of BO inhomogeneities and gradient nonlinearities. In *Proceedings of the 28th Annual Meeting of ESMRMB, Leipzig, Germany, 2011.* p. 604.
- [24] Hudson HM, Larkin RS. Accelerated image reconstruction using ordered subsets of projection data. *IEEE Trans Med Imaging* 1994;13(4):601–609.
- [25] Boellaard R. Standards for PET image acquisition and quantitative data analysis. *J. Nucl. Med.* 2009;50 Suppl 1:11S–20S.
- [26] Tylski P, Stute S, Grotus N, Doyeux K, Hapdey S, Gardin I, Vanderlinden B, Buvat I. Comparative assessment of methods for estimating tumor volume and standardized uptake value in (18)F-FDG PET. *J. Nucl. Med.* 2010;51(2):268–276.
- [27] Keyes J W. SUV: standard uptake or silly useless value? *J. Nucl. Med.* 1995;36(10):1836–1839.
- [28] Visser EP, Boerman OC, Oyen WJ. SUV: from silly useless value to smart uptake value. *J. Nucl. Med.* 2010;51(2):173–175.
- [29] Zhou A, Murillo H, Peng Q. Novel segmentation method for abdominal fat quantification by MRI. *J Magn Reson Imaging* 2011;34(4):852–860.
- [30] Zenge MO, Ladd ME, Quick HH. Novel reconstruction method for three-dimensional axial continuously moving table whole-body magnetic resonance imaging featuring autocalibrated parallel imaging GRAPPA. *Magn Reson Med* 2009;61(4):867–873.
- [31] Blumhagen JO, Ladebeck R, Fenchel M, Scheffler K, Quick HH. MR-based FoV extension in Whole-Body MR/PET Using Continuous Table Move. In *Proceedings of the 20th Annual Meeting of ISMRM, Melbourne, Australia, 2012.*

- [32] Braun H, Ziegler S, Paulus DH, Quick HH. Hybrid PET/MRI imaging with continuous table motion. *Med Phys* 2012;39(5):2735–2745.

Chapter 6

Summary and Conclusion

Summary

In this thesis, a new method in whole-body MR/PET hybrid imaging was developed and validated. Typical truncation artifacts at the edge of large MR FoVs were removed. As a result the MR-based attenuation correction was improved significantly and the reported bias in PET quantification was reduced.

The B_0 inhomogeneity and the nonlinearity of the gradient field are well known as the major causes for hardware-dependent distortions. Since the region of interest is usually within the specified FoV, the distortions for this specific region are usually small. In this work, the distortions were analyzed for regions of interest outside the usual specified FoV. Simulations were performed based on measurements of the main magnetic field and the gradient field. The simulations were in good agreement with phantom experiments. While the observed distortions are in the order of mm within the specified FoV, the distortions increased with increasing distance from iso-center and could reach up to several centimeters.

A dependency of the in-plane distortion on the readout gradient amplitude was observed in the frequency-encoding direction. The distortion due to the B_0 inhomogeneity was inversely proportional to the gradient amplitude whereas the distortion due to the nonlinearity of the gradient field was independent of the gradient. Thus, an optimal gradient amplitude corresponding to minimal residual distortion was found. The gradient nonlinearity was compensated by the B_0 inhomogeneity. The optimal gradient amplitude was space-dependent and varied with slice position and in-plane position. It was shown in simulations and volunteer measurements that a successful distortion reduction was feasible using one single optimal gradient amplitude for a region of interest as large as the cross-section of a typical patient's arm. Thus, the proposed imaging technique achieved a bi-lateral extension of the MR-based FoV.

The implementation of the FoV extension approach in a multi-slice spin-echo-based sequence allows for acquisition times that are realistic in clinical routine. The calculation and application of the optimal gradient amplitude was performed inline and for each slice position. No further user interactions or hardware changes were required. Furthermore, the bipolar dual-echo implementation obviated the separate measurement of the left and the right patient's arm. Finally, with the combination of the proposed acquisition technique with continuous table movement, full coverage of the patient's arm resting along the body was achieved. The patient's body was slid through the optimal slice position causing minimal residual distortion. No further interpolation between slices was needed.

The impact of the achieved MR-based FoV extension on the PET quantification was verified in a patient study. Typical truncation artifacts in the attenuation correction maps were removed. The improved attenuation correction reduced the reported bias in the PET quantification due to FoV limitations. Thus, the

results were in good agreement with PET-based or CT-based attenuation correction approaches.

Conclusion

A novel method in MR/PET was developed and validated. The MR-based FoV was significantly extended. Multiple acquisition approaches were implemented. Finally, the improvement on the PET quantification was verified. In comparison with PET-based approaches, the presented algorithm is purely MR-based and thus also applicable to specialized PET tracers with little uptake in the arms. Furthermore, the method might also be of interest for dynamic PET acquisitions for special applications such as oncology and cardiology with uptake distributions varying over time.

Acknowledgments

The University of Basel and the Siemens AG gave me the opportunity to perform my doctorate at the R&D headquarter for Magnetic Resonance in Erlangen. This exceptional situation allowed me for both working on fascinating topics of high interest for industry and analyzing and implementing different approaches in an academic way. During these studies, I worked together with various people supporting my ideas, supervising me, sharing their knowledge, and being open for discussions. These people I'm very grateful.

First of all, I thank my supervisor, Prof. Klaus Scheffler, for providing his knowledge and motivating me with his enthusiastic interest in my work.

Jürgen Kampmeier provided me this fascinating topic. He always trusted in my ideas. I thank him for supporting me.

With Ralf Ladebeck and Matthias Fenchel, I met regularly for inspiring discussions and brainstormings. I thank them for their excellent help in giving all my ideas a go even if they sounded unusual.

Professor Harald Quick revised several publications arising from this thesis. Furthermore, he and the involved staff of the Institute of Medical Physics and the University Hospital Erlangen made the patient study possible. I thank him for this support.

Thanks to all colleagues for answering my questions, particularly the MR/PET team, the gradient team and the physics team.

Furthermore, I would like to thank all Ph.D. students working at the MR department, particularly Antje and David, for creating an animate academic atmosphere and for volunteering to be measured.

I acknowledge Siemens Healthcare for the financial support and providing the access to a multitude of research and clinical MRI imaging systems.

Finally, but not less important, I thank my wife Francisca for the creative discussions and our son Niklas for showing me again and again how easy work gets with a baby smile in mind.

List of Abbreviations

ACF	Attenuation Correction Factors
CT	Computer Tomography
CTM	Continuous Table Movement
FDG	Fluorodeoxyglucose
FoV	Field-of-View
FT	Fourier-transform
GE	Gradient Echo
HASTE	Half Fourier Acquisition Single Shot Turbo Spin Echo
HUGE	B_0 Homogenization Using Gradient Enhancement
LAC	Linear Attenuation Coefficients
MIP	Maximum Intensity Projection
MLAA	Maximum-likelihood a-posteriori Algorithm
MRI	Magnetic Resonance Imaging
NMR	Nuclear Magnetic Resonance
OP-OSEM	Ordinary Poisson Ordered-Subsets Expectation-Maximization
PE	Phase Encoding
PET	Positron Emission Tomography
RF	Radiofrequency

RO	Readout
SAR	Specific Absorption Rate
SE	Spin Echo
SL	Slice Thickness
SS	Slice Selection
SUV	Standardized Uptake Value
TE	Echo Time
TR	Repetition Time

Academic Curriculum Vitae

Personal Data

Name: Jan Ole Blumhagen
Date of Birth: 15. September 1982
Place of Birth: Lübeck, Germany



University Education

06/2009 - 07/2012 Ph.D. Thesis, University of Basel and Siemens Healthcare. Supervisor: Prof. Dr. Klaus Scheffler.
10/2004 - 04/2009 Graduate Studies in Physics, University of Heidelberg, Specialization: Medical Physics, Degree: *Diploma* (Mark: "sehr gut")
03/2008 - 03/2009 Diploma Thesis, University Hospital Basel, (Mark: "sehr gut")
10/2002 - 08/2004 Undergraduate Studies in Physics, University of Kiel, Degree: *Intermediate Diploma* (Mark: "sehr gut")

Study Abroad

10/2005 - 06/2006 Imperial College London,
Degree: *Imperial College International Diploma*.

Scholarships and Student Program

01/2010 - 07/2012 Ernst von Siemens Doctoral Scholarship
10/2006 - 03/2009 TOPAZ - The Siemens Student Program
10/2005 - 06/2006 Foreign Scholarship for Study Abroad at Imperial College London